A New Crater Near InSight: Implications for Seismic Impact Detectability on Mars

I. Daubar, P. Lognonné, N. Teanby, G. Collins, J. Clinton, S. Stähler, A. Spiga, F. Karakostas, S. Ceylan, M. Malin, et al.

A New Crater Near InSight: Implications for Seismic Impact Detectability on Mars

Authors:

I. J. Daubar, Department of Earth, Environmental, and Planetary Sciences, Brown University, Campus Box 1846, Providence, RI 02912-1846, USA. *Corresponding author.* Ingrid_daubar@brown.edu
P. Lognonné, Université de Paris, Institut de physique du globe de Paris, CNRS, F-75005 Paris, France
N. A. Teanby, School of Earth Sciences, University of Bristol, Wills Memorial Building, Queens Road, Bristol BS8 1RJ, UK
G. S. Collins, Department of Earth Science and Engineering, Imperial College London, South Kensington Campus, London SW7 2AZ, UK
J. Clinton, Swiss Seismological Service (SED), ETH Zurich, Sonneggstr. 5, 8092 Zurich, Switzerland
S. Stähler, Institute of Geophysics, ETH Zürich, Sonneggstrasse 5, 8092 Zürich, Switzerland
A. Spiga, Laboratoire de Météorologie Dynamique / Institut Pierre Simon Laplace (LMD/IPSL), Sorbonne Université, Centre National de la Recherche Scientifique (CNRS), École Polytechnique, École Normale Supérieure (ENS), Campus Pierre et Marie Curie BC99, 4 place Jussieu, 75005 Paris, France
F. Karakostas, University of Maryland, College Park, Department of Geology, 8000 Regents Dr., College Park, MD, 20782-4211, USA
S. Ceylan, Institute of Geophysics, ETH Zurich, Sonneggstr. 5, 8092 Zurich, Switzerland
M. Malin, Malin Space Science Systems, San Diego, CA
A. S. McEwen, University of Arizona. Tucson, AZ
R. Maguire, University of Maryland, College Park, Department of Geology, 8000 Regents Dr., College Park, MD, 20782-4211, USA
C. Charalambous, Department of Electrical and Electronic Engineering, Imperial College London, South Kensington Campus, London, SW7 2AZ, United Kingdom
K. Onodera, Université de Paris, Institut de physique du globe de Paris, CNRS, F-75005 Paris, France
A. Lucas, Université de Paris, Institut de physique du globe de Paris, CNRS, F-75005 Paris, France
L. Rolland, Université Côte d'Azur, Observatoire de la Côte d'Azur, CNRS, IRD, Géoazur, 250 av Einstein, 06560, Valbonne, France
J. Vaubaillon, Observatoire de Paris, IMCCE, PSL, 77 Av Denfert Rochereau, 75014 Paris, France
T. Kawamura, Université de Paris, Institut de physique du globe de Paris, CNRS, F-75005 Paris, France
M. Böse, Swiss Seismological Service (SED), ETH Zurich, Sonneggstr. 5, 8092 Zurich, Switzerland
A. Horleston, School of Earth Sciences, University of Bristol, Wills Memorial Building, Queens Road, Bristol BS8 1RJ, UK

M. van Driel, Institute of Geophysics, ETH Zurich, Sonneggstr. 5, 8092 Zurich, Switzerland
J. Stevanović, AWE Blacknest, Aldermaston, Reading, GR7 4RS, UK
K. Miljković, Space Science and Technology Centre, School of Earth and Planetary Sciences, Curtin University, GPO Box U1987, Perth, WA 6845, Australia
B. Fernando, Department of Earth Sciences, University of Oxford, South Parks Road, Oxford OX1 3AN, United Kingdom
Q. Huang, Department of Geology, University of Maryland, College Park, 8000 Regents Dr., College Park, MD, 20782-4211, USA
D. Giardini, Institute of Geophysics, ETH Zurich, Sonneggstr. 5, 8092 Zurich, Switzerland
C. S. Larmat, Los Alamos National Laboratory, PO Box 1663, Los Alamos, NM 87545, USA
K. Leng, Department of Earth Sciences, University of Oxford, South Parks Road, Oxford OX1 3AN, UK
A. Rajšić, Space Science and Technology Centre, School of Earth and Planetary Sciences, Curtin University, GPO Box U1987, Perth, WA 6845, Australia
N. Schmerr, University of Maryland, College Park, Department of Geology, 8000 Regents Dr., College Park, MD, 20782-4211, USA
N. Wójcicka, Department of Earth Science and Engineering, Imperial College London, South Kensington Campus, London SW7 2AZ, UK
T. Pike, Department of Electrical and Electronic Engineering, Imperial College London, South Kensington Campus, London, SW7 2AZ, United Kingdom
J. Wookey, School of Earth Sciences, University of Bristol, Wills Memorial Building, Queens Road, Bristol BS8 1RJ, UK
S. Rodriguez, Université de Paris, Institut de physique du globe de Paris, CNRS, F-75005 Paris, France
R. Garcia, Institut Supérieur de l'Aéronautique et de l'Espace SUPAERO, 10 Avenue Edouard Belin, 31400 Toulouse, France
M. E. Banks, NASA Goddard Space Flight Center, 8800 Greenbelt Road, Greenbelt, MD 20771, USA
L. Margerin, Institut de Recherche en Astrophysique et Planétologie, Université Toulouse III Paul Sabatier, CNRS, CNES, 14 Av. E. Belin, 31400, Toulouse, France
L. Posiolova, Malin Space Science Systems, San Diego, CA
B. Banerdt, Jet Propulsion Laboratory, California Institute of Technology, Pasadena, CA 91109, USA

Key Points

- A new 1.5 m diameter impact crater formed on Mars ~40 km from the InSight lander between February and April 2019.
- Three candidate seismic events occurred during this time frame, but none of them can be definitively associated with the new crater.
- We revise our expectations for InSight impact detections above the background noise to be ~2 per Earth year, with large uncertainties.

Index terms:

5420 PLANETARY SCIENCES: SOLID SURFACE PLANETS - Impact phenomena, cratering (6022, 8136)
7299 SEISMOLOGY - General or miscellaneous
8136 TECTONOPHYSICS - Impact phenomena (5420, 6022)

Abstract

A new 1.5 meter diameter impact crater was discovered on Mars only ~40 km from the InSight lander. Context camera images constrained its formation between February 21 and April 6, 2019; follow-up HiRISE images resolved the crater. During this time period, three seismic events were identified in InSight data. We derive expected seismic signal characteristics and use them to evaluate each of the seismic events. However, none of them can definitively be associated with this source. Atmospheric perturbations are generally expected to be generated during impacts; however, in this case, no signal could be identified as related to the known impact. Using scaling relationships based on the terrestrial and lunar analogs and numerical modeling, we predict the amplitude, peak frequency, and duration of the seismic signal that would have emanated from this impact. The predicted amplitude falls near the lowest levels of the measured seismometer noise for the predicted frequency. Hence it is not surprising this impact event was not positively identified in the seismic data. Finding this crater was a lucky event as its formation this close to InSight has a probability of only ~0.2, and the odds of capturing it in before and after images is extremely low. We revisit impact-seismic discriminators in light of real experience with a seismometer on the martian surface. Using measured noise of the instrument, we revise our previous prediction of seismic impact detections downwards, from ~a few to tens, to just ~2 per Earth year, still with an order of magnitude uncertainty.

Plain Language Summary

A small new impact crater was discovered on Mars very close to the InSight lander. Photographs from a camera in orbit show it formed between February 21 and April 6, 2019. Three seismic events were detected by InSight during this time. We estimate what seismic data from the impact would have looked like and whether or not each of the seismic events was caused by the new impact, but none of them can be definitely linked. We predict the size, frequency, and length of time of the signal that would have come from this impact. Even though this impact is very close to InSight, it's small, so it was not a large seismic event. The signal would be near the quietest the instrument ever gets. There is only a 1 in 5 chance per Earth year that a crater would have formed this close to InSight, and a much lower chance that it would be imaged, thus we were very lucky to find this crater. Using what we know about the instrument on the ground, we update the number of impacts we expect to find with InSight to ~2 each Earth year, with a lot of uncertainty.

1 A new impact constrained by orbital images

On April 6, 2019, an image taken by the Context camera (CTX; Malin *et al.,* 2007) on the Mars Reconnaissance Orbiter (MRO) revealed a new dark spot that was not present in a previous image taken on February 21 (Fig. 1), only ~40 km from the newly-landed InSight mission (Interior Exploration using Seismic Investigations, Geodesy and Heat Transport; Smrekar *et al.,* 2019). Detecting an impact in both seismic data and orbital images would be an exciting development, leading to a number of scientific advances (Daubar *et al.*, 2018). This would be a seismic source with a known location, and thus a known distance and direction. A certain location and depth would allow modeling of seismic ray paths through the interior that could constrain seismic velocities and the physical properties of the material through which the rays traveled. This would improve models of interior structure and the seismic attenuation of Mars. An impact clearly observed in both orbital and seismic data would also provide a calibration of the seismic source parameters such as moment, cutoff frequency, and seismic efficiency (the ratio of impact energy to radiated seismic energy). The seismic efficiency, for example, is not well constrained, with values in the literature ranging from 10^{-6} to 10^{-2} (Daubar *et al.*, 2018 and references therein). High resolution images of newly formed craters would characterize crater sizes, leading to an empirical relationship between impact size and observed seismic amplitudes. Enough such observations would also result in an independent measurement of the current impact rate, anchoring absolute bombardment rates. Thus identifying an impact in seismic data that was also imaged from orbit would satisfy many important scientific goals. So naturally, this event was of immediate interest to the InSight team.

A high-resolution 25 cm pixel scale image from the High Resolution Imaging Science Experiment (HiRISE; McEwen *et al.,* 2007) was acquired shortly thereafter. The HiRISE image resolved a ~1.5 meter diameter impact crater at the location of the new dark spot (Fig. 1D), showing that an impact event occurred in the short period of time constrained by the before and after CTX images, between 21 February (03:56:17 UTC) and 6 April (08:19:17 UTC) in 2019. This occurrence is not especially rare; ~900 new dated impacts have been discovered in the last ~decade on Mars using similar techniques (Malin *et al.,* 2007; Daubar *et al.,* 2013), although the imaging date constraints are usually on the order of a few years rather than a month. This impact was also extraordinary in its location very close to the recently-landed InSight mission. At this distance, the prospect of detecting the impact event using the seismic and atmospheric instrumentation on InSight was an exciting possibility. This is the only impact we know to have formed this close to the lander during the time since InSight landed on Mars on 26 November 2018.

The new crater is located at 3.866°N planetocentric latitude, 135.613°E longitude, just 37.36 km from InSight, which landed at 4.502°N, 135.623°E (Parker *et al.*, 2019). It is located along an azimuth of 180.9°, almost directly south of the lander. The asymmetric low-albedo blast zone pattern around the crater (Fig. 1D), caused by the disturbance of light-toned dust during the impact, indicates a somewhat oblique impact coming from the southwest direction. Small dark spots to the southwest of the crater could be blast zones around secondary craters or multiple smaller primary craters in a clustered impact that formed when the impactor fragmented in the atmosphere (Daubar *et al.,* 2019). Craters within these smaller dark spots are not resolved. The pattern of dark spots is more consistent with a clustered impact than with secondary craters;

secondary craters would be concentrated downrange rather than uprange, and typically have more symmetric radial patterns. In either case, the contribution of the group of smaller craters to a combined seismic signal would be negligible compared with that of the main ~1.5 m diameter crater (Schmerr *et al.,* 2019).

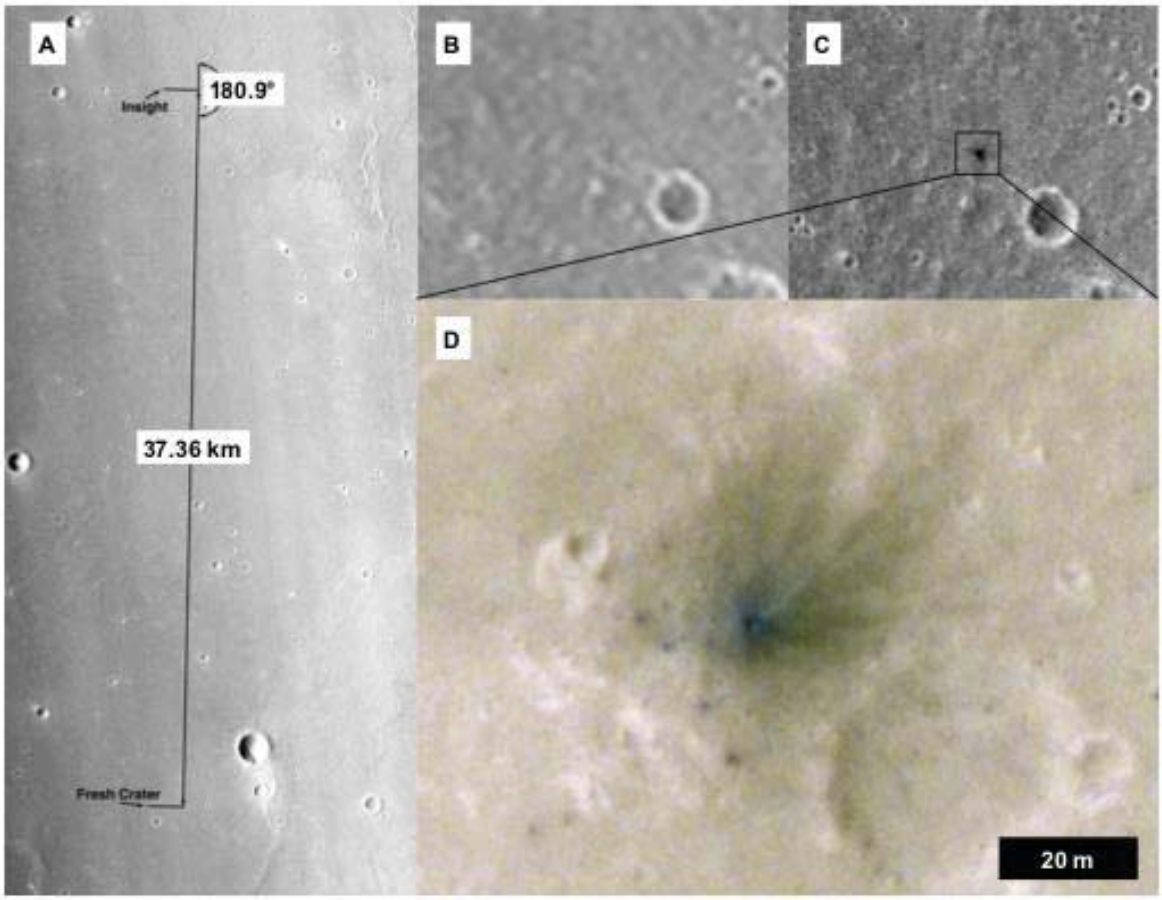

Figure 1.

New crater observations. (A) CTX context image showing locations of InSight lander and new dated impact. (B) CTX image K14_068929_1845_XN_04N224W_190221 taken February 21, 2019 (6 m/px). (C) CTX image K16_059495_1829_XN_02N224W_190406 taken April 6, 2019, showing new dark spot that was not present in previous image. (D) Cutout from HiRISE image ESP_060128_1840 (COLOR RDR; 25 cm/px) showing new impact crater. North is up, and images have been stretched for contrast. Image credits: NASA/JPL/MSSS (CTX); NASA/JPL/University of Arizona (HiRISE).

A second HiRISE image was acquired to obtain stereo data, but the crater is not resolved in the resulting Digital Terrain Model (DTM). (See anaglyph in Fig. S1.) A depth of a few tens

of centimeters is estimated for the new crater. Although this depth is not resolved in the DTM, an estimate was possible by scaling from larger, resolved, craters in the DTM.

In subsequent sections we derive the expected seismic and atmospheric signals that would have been produced by this known impact and have the potential to have been detected by InSight (Section 2). In Section 3, we describe the search of the seismic data during the time period constrained by the before and after CTX images, and the three candidate seismic events that were found. We then evaluate which of those seismic events, and any associated atmospheric signals, might be connected with the formation of the new crater. Finally, in Section 4, we use InSight mission experience thus far to re-evaluate the seismic impact discriminators we identified before landing, and we present updated expectations for impact detections with InSight in light of real data acquired since landing.

2 Predicted signals from the new impact crater

2.1 Predicted impact parameters from the observed crater

To assess the detectability of the observed ~1.5 m diameter crater by InSight, we first estimate the impactor parameters. The geology of the impact target area is very similar to that in the immediate vicinity of the InSight lander, which has been characterized in detail (Golombek *et al.*, 2020). The material in which the crater formed is likely to be a loose, porous regolith with very low cohesive strength ($\lesssim$50 kPa). The diameter of meter-scale impact craters formed in such a material is expected to scale as a power of the vertical impactor momentum, with only minor additional dependence on other impactor parameters (Holsapple, 1993; Holsapple and Housen, 2007). For a 1.5±0.25 m diameter crater, the predicted vertical impactor momentum is 100-3000 Ns, depending on the cohesive strength of the regolith (Fig. S2). The lower limit applies if the martian regolith can be represented as cohesionless dry sand; a nominal upper limit applies if the martian regolith has an effective cohesive strength of 50 kPa. An even higher impactor momentum is possible, but that would require a cohesive strength of a well-cemented terrestrial soil, which is not compatible with observations of the martian regolith made in the vicinity of the InSight lander (Golombek *et al.*, 2020).

The seismic source of the impact can be expressed as an equivalent seismic moment, which scales approximately linearly with impactor momentum according to two independently derived, semi-empirical scaling relationships (Shishkin, 2007; Gudkova et al. 2011, 2015; reviewed in Daubar *et al.*, 2018). For an impactor momentum of 100-3000 Ns, these relationships predict an equivalent seismic moment of 10^6-10^7 Nm (Fig. S3).

The estimated impactor momentum implies an impactor mass ~0.1 to ~1 kg, depending on impact speed. Meteoroids in this mass range are substantially decelerated by Mars' atmosphere (Fig. S4) and are predicted to lose approximately 90% of their initial kinetic energy, 75% of their initial speed, and 30% of their initial mass by ablation and drag before striking the ground (Table S1). Thus vertical impact speeds at the ground in the range of only 1-3 km/s are expected for typical pre-entry meteoroid encounter speeds of 5-15 km/s (Le Feuvre and Wieczorek, 2008; JeongAhn and Malhotra, 2015) and entry angles of 15-90°. At these relatively

slow impact speeds, and taking into account the uncertainty in impactor momentum, estimates of the impact energy range from approximately 0.1 MJ to 2 MJ (see supplemental section S1).

An independent test of these energy estimates is provided by the empirical relationship from Teanby and Wookey (2011) between crater diameter (D) and impact energy (E), based on laboratory and field impact experiments, explosive analogues, and the Apollo artificial lunar impacts:

$$D = 8.8^{+2.6}_{-3.5} \times 10^{-3} E^{0.32\pm0.01} \left(\frac{g_\oplus}{g}\right)^{3/16}, \quad (1)$$

where $g_\oplus$ is Earth's gravity (9.81 ms^{-2}) and g is Mars' gravity (3.73 ms^{-2}). The error bars incorporate scatter in the source data and the uncertainties in impact conditions. Using this relationship gives an estimated ground impact energy of 5.3±1.8 MJ, which is somewhat larger than our previous estimate. We attribute this difference to the fact that most of the data used to construct Eq. (1) are from experiments in terrestrial soils and rocks that have a much higher cohesive strength than the strength we adopt for the martian regolith based on in situ and remote sensing of this region. Therefore, this scaling relationship provides an upper bound on the impact energy.

2.2 Predicted seismic signals based on energy and moment scaling

The estimated ground impact energy can be used to obtain a first order prediction of seismic P-wave amplitude v at source-receiver distance x using scaling relations developed for terrestrial impacts (Teanby, 2015):

$$v(x, E) = a x^b E^c \quad (2)$$

where scaling law constants a=5.6x10^{-5}, b=-1.6, and c=0.5 under Mars conditions (Teanby, 2015). The overall uncertainty on $v(x, E)$ is a factor of four. This relationship is strictly only valid over the range of energies and distances used by Teanby (2015), which cover ~400-10,000 kg TNT equivalent (~2x10^3-4 x10^4 MJ) (excluding the very high energy buried nuclear explosions) and 0.5-1200 km ranges. These events had peak seismic frequencies in the range 1-16 Hz, with the Apollo lunar and Carancas Earth impacts peaking from 1-10 Hz. We can also estimate the longest timescale in the source function using crater excavation timescale, τ=√(D/g) ~0.6 s, implying a frequency content of >1 Hz. Therefore, the scaling relationship is a reasonable, although not ideal, match to conditions for the new martian crater, with the P-wave frequency content likely peaking at a few Hz or slightly higher.

A first order prediction of seismic P-wave amplitude v for the new event is shown in Figure 2 compared to the range of measured InSight noise levels in the 1-16 Hz bandpass from Lognonné *et al.* (2019, 2020). The estimated P-wave amplitude at the observed range of 37 km is 0.8-4x10^{-9} ms^{-1} for 0.1-2.0 MJ and 6x10^{-9} ms^{-1} with a factor of four uncertainty for the 5.6 MJ upper bound. Furthermore, Wójcicka *et al.* (2020) use numerical impact simulations to propose a recasting of the amplitude scaling in terms of impact momentum instead of energy, which relates

to seismic moment more closely to linearly. When applied to impacts in relevant analog materials, this recasting results in a reduction in predicted seismic amplitudes by up to two orders of magnitude for small craters. Overall, these scaling laws have large uncertainties, and predictions span three orders of magnitude, but all imply a modest signal-to-noise ratio (SNR), with a likely SNR of only ~1 on average. These amplitude estimates are also in reasonable agreement with peak ground velocities predicted from numerical waveform simulations of the impact event (see supplemental section S2). During the detection period, the continuous seismometer data coverage is limited to 10 sps (5 Hz Nyquist) sampling except during exceptional periods where 20 sps or 100 sps was collected (Fig. S10). Therefore, any seismic energy over 5 Hz is unlikely to have been recorded for the majority of the time in question. The combination of low SNR, high frequency content, and low sample rate implies this event would have been be very difficult to detect seismically.

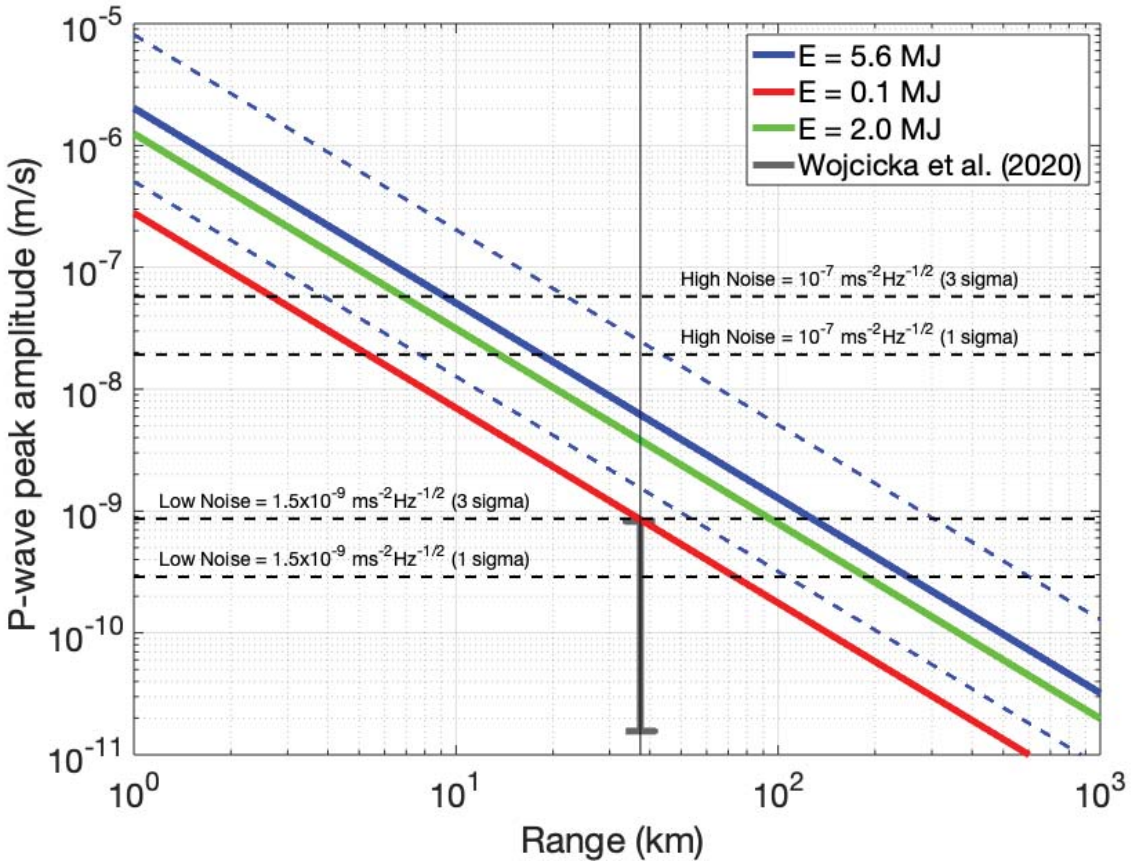

Figure 2.

Estimated amplitude of P-wave signal from the 1.5 m diameter new impact. The amplitude is estimated using the impact energy scaling relationship from Teanby (2015) in equation (2) as described in the text. Solid lines show nominal amplitude prediction from scaling relations and uncertainty for three potential impact energies, a nominal range (red to green) and an upper limit (blue). Dashed blue lines show uncertainty on the upper limit E=5.6 MJ case. Horizontal

dashed lines show range of seismic noise measured at 4 Hz at the InSight landing site for 1 and 3 sigma (Lognonné et al., 2019, 2020), and vertical black line shows the distance between InSight and the new crater. Gray vertical bar shows range of predictions from Wójcicka et al. (2020) from numerically derived impact momentum scaling. Seismic noise amplitudes are converted to equivalent velocities by integrating the amplitude spectral density (ASD) noise for the 1-16 Hz bandwidth, using equation 14 in Teanby (2015). Amplitude estimates for the observed impact are at or below the noise levels.

2.3 Predicted seismic signals based on lunar impact analogies

The closest seismic analog for this impact is the Lunar Module of Apollo 14 (LM), which impacted 67 km from the Apollo Lunar Surface Experiments Package (ALSEP) station of Apollo 14. Its amplitude was about 40 data units (DU) on the vertical Long Period (LP) axis in peaked mode, corresponding to 2 nm of ground displacement at 2 sec. See Lognonné *et al. (*2009) for a detailed analysis of this and other lunar impacts.

At such a small epicentral distance, intrinsic attenuation can be neglected, and the seismic signal is mostly constrained by the elastic propagation properties, which are mostly diffusive on the Moon, and the source parameters. These parameters are summarized in Table 1.

Impact	**Distance from seismometer (km)**	**Velocity (km/s)**	**Angle (° from vertical)**	**Mass (kg)**	**Mv (Mv_z) (kg m/s)**	**Rim Diam (m)**	**Depth (m)**	**Formation time**
LM impact on the Moon	**67**	**1.68**	**86.4°**	**2383**	$4x10^6$ ($2.5x10^5$)	6.5	1.37	0.94 sec
New 1.5-m crater on Mars	**37.4**	1-3	Not well constrained; moderately oblique	0.1-1	$1.4 x10^2$-$4.3 x10^3$ ($1x10^2$-$3x10^3$)	**1.5**	A few tens of cm	~0.30-0.35 sec

Table 1.

Comparison between the source parameters of the Apollo 14 Lunar Module (LM) impact and the CTX-image-constrained impact that formed the new 1.5-m diameter crater discussed in this paper. Parameters from the LM impacts are from Lognonné et al. (2009) and references therein. A 45° impact angle is assumed for the martian impact, although this is only weakly constrained. Formation time is estimated from Holsapple (1993) and using $0.5\sqrt{(D/g)}$ as an estimate of the

crater growth time (Schmidt and Housen, 1987). Known values are given in bold, other values are inferred.

According to Sato and Korn (2007), the maximum amplitude of a pulse propagating in the multiple forward scattering regime is proportional to $\sqrt{\frac{1}{xT_m}}$, where *x* is the hypocentral distance and T_m is a characteristic time scale. T_m depends on the heterogeneity of the medium as:

$$T_m = \sqrt{\pi}\frac{<\varepsilon^2>D^2}{2\alpha\beta} \quad (3)$$

Where β is the wave propagation speed, α is the correlation length of the random fluctuations, and their variance is $< \varepsilon^2 >$. This theory predicts that the typical maximum amplitude is proportional to $\sqrt{\frac{\alpha\beta}{x^3<\varepsilon^2>}}$. Note these formulae are valid in media with velocity and density with gaussian fluctuations (Sato and Korn, 2007).

We do not expect the correlation distance to differ significantly between Mars and the Moon, but fluctuations are certainly stronger on the Moon because scattering is stronger. As the diffusivity is inversely proportional to $< \varepsilon^2 >$, we expect the amplitude to be 5 to 10 times larger on Mars than on the Moon, for the same source and distance, following initial comparisons of the crustal diffusivity (Lognonné *et al.*, 2020).

With these assumptions, we can convert amplitudes of impacts detected on the Moon to the martian situation. Following previous work (Lognonné *et al.*, 2009; Gudkova *et al.,* 2011; 2015), we assume that the amplitude of the signal is linearly related to the vertical momentum, which implies a source for the martian impact smaller in moment than the LM source by a factor of ~83-2500. On the other hand, the difference in diffusion makes the maximum amplitude of the signal larger by a factor 5-10. Last but not least, the difference in distance for the LM impact at 67 km makes the signal larger by a factor of 2.37 for an -1.5 exponential decay, comparable to the -1.6 power law decay of local magnitudes on Earth at short distance (Richter, 1958). Combining these factors, this suggests a martian signal smaller than the lunar one by a factor of 8.3-500 without a geometrical spreading correction; with that correction, it would be smaller by a factor of 3.5-210.

The duration of the signal can also be addressed with similar analogies. Martian signals are expected to have much shorter durations than lunar ones due to the ratio of diffusivities. Rise times are found to be in the range of 600-800 sec for lunar impacts (Gillet *et al.*, 2017) and are expected to be reduced by a factor of 30-100 for Mars. Signals with SNR of 3 will have durations of about 2-3 times the rise time, leading to durations in the range of 20-60 seconds for each phase in this case.

In summary, based on early estimates of the diffusivity of Mars, we expect this impact on Mars to have a signal smaller in amplitude by a factor of 3.5 to 210 compared to the Apollo 14

LM impact recorded by the Apollo 12 vertical LP instrument. Martian impact signals are also expected to have much shorter durations of ~20-60 seconds.

In order to estimate propagation time differences between the main phases, we use the fact that an event at a distance of 37 km in a homogenous martian crust will propagate down to a depth of ~500 m. We can expect that most of the energy of this event will therefore be guided in the first half km of depth, for which seismic velocities are expected up to 2000 m/s for P waves and 1000 m/s for S waves. Most of the energy will be in surface waves, for which typical group velocities are computed with Mineos software (https://geodynamics.org/cig/software/mineos/) (Fig. 3a). These are shown for one possible model of the shallow subsurface structure based on constraints proposed by Lognonné *et al.* (2020) for the first five meters of depth, measurements of the seismic velocities of layers of volcanic material (Lesage *et al.*, 2018) down to 1 km depth, and the TAYAK reference model below that (Smrekar *et al.*, 2019). See supplemental section S3 for details of the model. Note that apart from the first five meters, this model is merely representative, constrained only by earth analog. Propagation times (Fig. 3b) range from 11-15 sec to 80 sec for the four first spheroidal/toroidal surface wave branches. We note that the ratio between the fundamental and the harmonic group velocities can be much larger than the standard $\sqrt{3}$ ratio between the velocities of P and S body waves used by MQS (see Section 3). As an example, the 78 seconds between the two phases of event S0116a (discussed in section 3.1) are compatible with a slow packet propagating at 360 m/s (roughly the shear wave velocity at the base of the bedrock in our model) and a second packet propagating four times faster, which is roughly the P-wave velocity at a depth of ~100 meters, as proposed by Lesage *et al.* (2018). A difference of several minutes between the arrival of the first and second pulse is also found in event S0105a (see section 3.1). Second arrivals such as these might also be fundamental scattered Rayleigh waves, while the first arrivals could be overtones propagating in the deeper bedrock. The group velocity of the subsurface models also shows a clear variation of the group velocity just above 0.5 Hz, which might be the reason the signal has a cutoff frequency ~0.5 Hz.

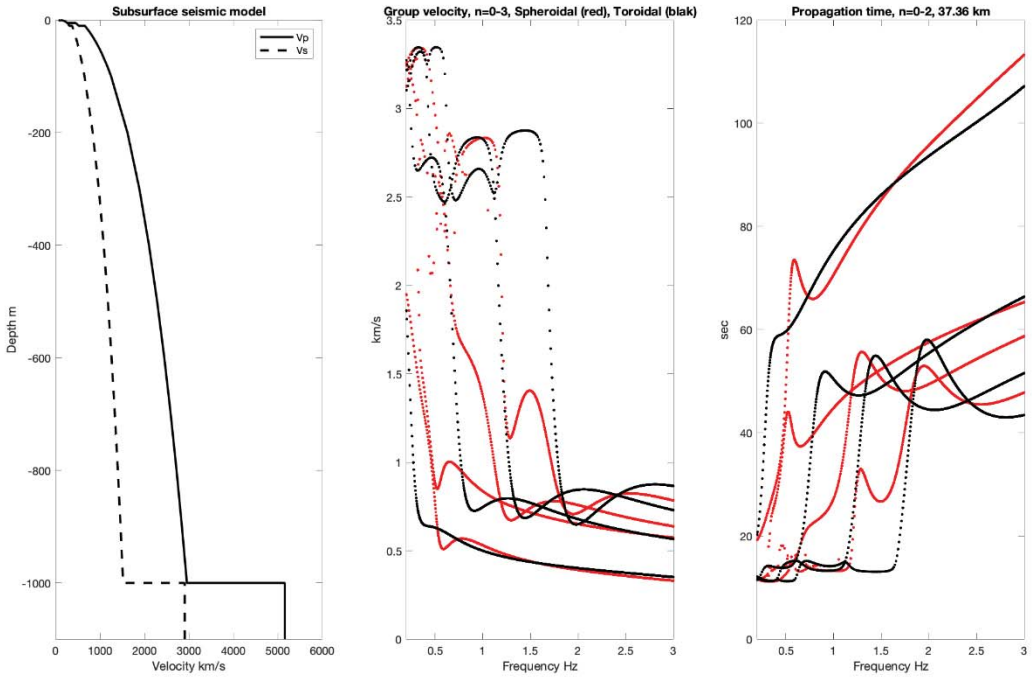

405

406 Figure 3.

407 *(Left) Subsurface seismic model. (Middle) Group velocities of the fundamental Rayleigh and*
408 *Love waves and of the three first spheroidal (red) and toroidal (black) overtones. (Right)*
409 *Propagation time of the surface wave packet to a distance of 37.36 km, as a function of*
410 *frequency up to 3 Hz. Model data is provided in Table S2.*
411

412 In summary, based on lunar data extrapolated to Mars, the shallow layers and diffusivity
413 of Mars suggests that for an event at the distance of the new crater, we expect phase durations of
414 30 sec to 1 minute, with differences in phase arrivals up to about one minute.
415

416 2.4 Predicted atmospheric signals

417

418 A meteor entering the atmosphere and causing an impact crater would generate at various
419 atmospheric levels in the entry path and at impact time both low-frequency gravity waves
420 (typically 0.01-0.001 Hz) and high-frequency acoustic waves (frequencies above 0.01 Hz,
421 typically 1-100 Hz) (Spiga *et al.*, 2018; Revelle 1976; Garcia *et al.*, 2017; Karakostas *et al.*,
422 2018). Those signals could be detected by a high-sensitivity pressure sensor operating
423 continuously such as the pressure sensor in the Auxiliary Payload Sensor Suite (APSS) on board
424 InSight (Daubar *et al.*, 2018).
425

426 An airburst signal would be characterized by two arrivals: first, the main seismic signal
427 of surface waves excited at the location of the impact; and second, the blast wave through the
428 atmosphere exciting the ground at the lander (Stevanović *et al.*, 2017). A differential travel time

of ~2 minutes is expected between two such signals due to the difference in wave propagation speeds of 230 m/s in the air and 1.5 km/s in the subsurface over the 37 km distance from the impact to the lander. Such a signal would be much smaller than InSight's pressure sensor limit of detectability, so SEIS would be the only way to detect such a phenomenon.

Atmospheric entry modeling demonstrates that for this scale of impact the majority of the meteoroid's kinetic energy is transferred to the atmosphere during deceleration and ablation, and only a small fraction is directly coupled to the ground by the surviving fragment(s). The relatively large blast zone surrounding the crater (Fig. 1D) is testament to this partitioning. However, previous work suggests that detection of the direct ground impact is more likely than detection of airburst-generated acoustic and gravity waves near the ground surface (Garcia *et al.,* 2017) as InSight's detection capability of acoustic and gravity waves produced by airbursts and surface explosions is negatively affected by atmospheric attenuation and propagation conditions less favorable than on Earth (Lognonné *et al.*, 2016). Moreover, numerical modeling (based on the methodology of Karakostas *et al.*, 2018) suggests that even in the endmember case of all the meteoroid kinetic energy being deposited in the atmosphere, the resulting air-coupled seismic waves would still not be detectable by the InSight instruments. Acoustic ray propagation models (Garcia *et al.*, 2017; Spiga *et al.*, 2018) show the trajectories of infrasound rays do not reach the InSight lander, which is in an unfortunate shadow zone at this distance from the impact (Fig. S11). Considering both atmospheric wave propagation conditions and meteor energy scaling, we therefore do not expect the acoustic and gravity waves generated by the meteoroid that formed the 1.5 m crater to be detected by InSight.

3 Candidate seismic events in the time period of interest

3.1 Description of SEIS data and the candidate events

The time between the before and after CTX images was a period of immense interest in the data coming from InSight. The most relevant data was from the seismometer, Seismic Experiment for Interior Structure (SEIS; Lognonné *et al.*, 2019). This temporal search window occurred as SEIS commissioning was being finalized, only a few weeks after SEIS was placed on the ground (17 January 2019) and the Wind and Thermal Shield (WTS) had been placed over it (2 February 2019), allowing the lowest possible noise on the instrument. Fortunately, continuous data collection (InSight Mars SEIS data service, 2020) had already transitioned to being round-the-clock, and three-component Very-Broad-Band (VBB) and Short-Period (SP) data at 10 sps, sometimes also at 20 sps, was available throughout the time period (Fig. S10).

Figure 4 provides an overview of the completeness, the noise, and the occurrence of seismic signals in the data within the search window. Seismic noise on Mars clearly falls into a daily pattern, with low noise only occurring between ~16:00 LMST (Local Mean Solar Time) to ~02:00 LMST (Lognonné *et al.*, 2020, Giardini *et al.*, 2020). Outside of this time, there is a substantial increase in noise, with steady winds in the early morning followed by a gusty midday period. During these times, only very strong seismic signals can be detected. Furthermore, not all days include a significant quiet period. Thus, there are large daily and day-to-day variations in

our capacity to detect weak seismic events on Mars using SEIS data. During the search window, we estimate weak signals could be reliably detected only ~30% of the time.

Despite these limitations to the data, three potential seismic events were identified between the times of the constraining CTX images (Fig. 4). Although all three are weak signals, there are unique aspects of these events that deserve examination. We discuss the characteristics of each of them, and the likelihood that each is the signal resulting from the observed new crater.

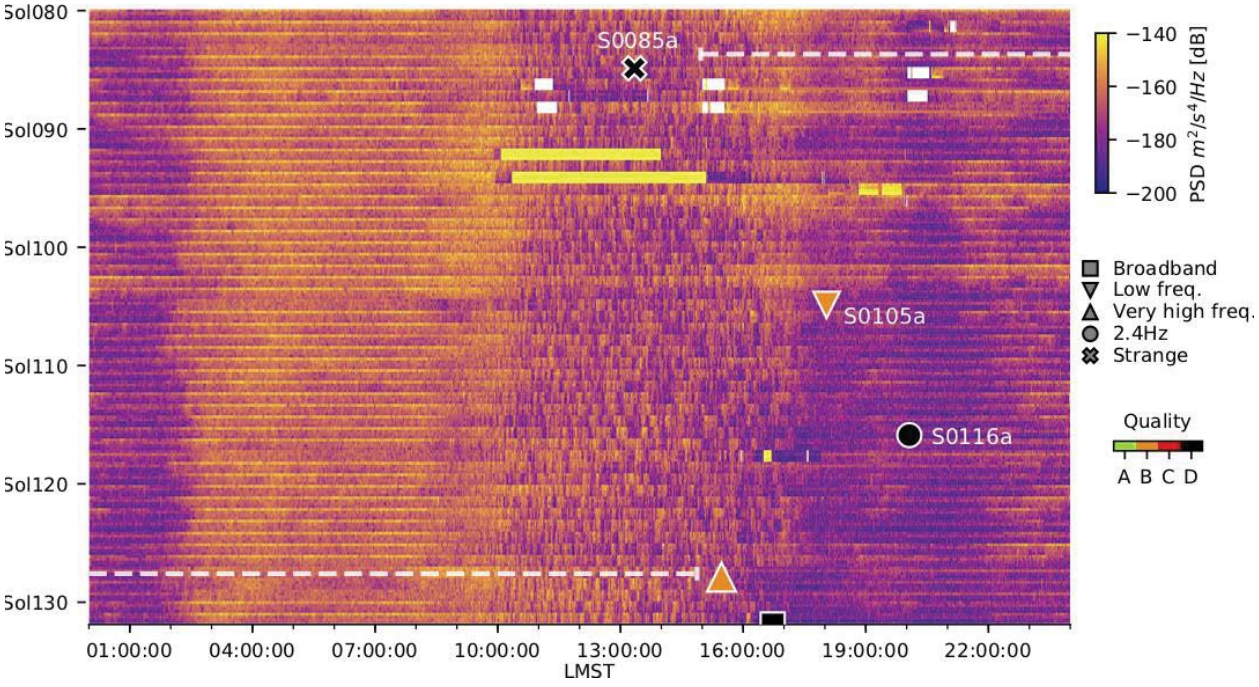

Figure 4.

Spectrogram stack from InSight sol 80 (16 February 2019) to sol 132 (10 April 2019). This period bounds the impact search window from sol 84 14:55 LMST (21 February 2019 03:56 UTC) to sol 127 14:18 LMST (6 April 2019 08:20 UTC), indicated by start/end of the white dashed lines. Each horizontal line in this plot corresponds to a sol-long acceleration spectrogram from 20 s to 4 Hz for the vertical VBB component. White and yellow bars indicate data gaps and amplitude saturation, respectively, occurring during sensor calibration and hammering of the heat flow probe. The three events detected and discussed in this paper are marked with symbols corresponding to the event type, while event quality is indicated by symbol color (see legend). Two events that occurred just after the end of the search window are also indicated.

The Marsquake Service (MQS, Clinton *et al.*, 2018) is tasked with reviewing all data from SEIS, detecting and characterizing seismic energy, and maintaining a catalogue of marsquakes. MQS detects events by careful manual review of all continuous data. Over the course of the mission so far, the most effective approach to identifying marsquakes has proven to be data review using spectrograms. Standard MQS operations produce daily spectrograms with a

window length of 50 seconds for frequencies below one Hz and 10 seconds for higher frequencies. In the first months, two major event families have been observed (Giardini *et al.*, 2020; InSight Marsquake Service, 2020). The first family is characterized by events with energy dominant at lower frequencies, visible as a 10-20 minute-long energy surplus between 0.1 and 3 Hz. This family comprises the two event types, Low Frequency (LF) and Broadband. The largest of these events (named S0173a and S0235b; Giardini *et al.*, 2020, Lognonné *et al.*, 2020) have clearly identifiable P- and S-waves, with clear polarization showing the direction as seen from the lander, followed by long codas of scattered energy. Smaller events of this type have polarities that are less clear or are not detectable, but the envelope of the waveforms and their spectral content supports the interpretation that they are smaller versions of the same type of event. The second major family includes High Frequency (HF) events, characterized by an energy content mainly above 1 Hz, an extended coda, and a lack of polarization. An additional curious feature of the InSight landing site is a local seismic resonance at 2.4 Hz. For larger HF events, the spectrum can be matched by a general earthquake spectrum, taking into account source size and attenuation, modulated by an amplification of 12 dB in spectral energy around 2.4 Hz. For smaller HF events, only this peak is visible, while the bulk of the energy is below the ambient noise level. Events in this family are classified as High Frequency, Very High Frequency, or 2.4 Hz. A handful of events have been documented as “Strange” if they do not fit into any of these standard event types.

During the time period of the impact search, one event was found during standard MQS operations. It has the label S0105a (the first seismic event to occur on sol 105 of the mission) and is a Low Frequency event. It was in fact the first seismic event detected during the whole mission. After the CTX discovery of the impact, a review of all data during this period was performed by the InSight team, both within and independently of the MQS team. This review took into account the improved understanding of marsquake character that had accumulated from other events in the meantime. During this review, two additional events in the time period were identified: a small High Frequency event on sol 116 and one unclassifiable seismic signal on sol 85. We first describe the three events in detail:

S0085a [2019/02/22 02:58:15 UTC, 13:35 LMST; MQS classification: Strange signal]

A summary of the S0085a event is shown in Figure 5. This event, which appears to be unique among events detected on InSight thus far, consists of a very narrow-banded energy surplus at 0.7 Hz, with a bandwidth of 0.05 Hz. There is a slight rise in frequency over the course of the event, from 0.57 Hz up to 0.7 Hz. The signal is visible dominantly on the north component, with weak traces in the Z (vertical) component. This indicates a clear N/S azimuth. The signal occurs only hours after the opening of the search window, during the part of the day with high atmospheric noise. In fact, it is interrupted by several wind bursts creating noise more than 10 dB above the signal itself. Because it can only be resolved during the intermittent quiet periods, the exact start and end times cannot be positively identified, but the event lasts at least 10 minutes. The very narrow bandwidth does not fit any expected seismic mechanism (including impacts). A similar signal has not been observed a second time during the mission, especially not during a quieter period, which would allow a better classification of its character. No particular lander activity was going on at the time of this event that could explain it. Given the high

546 atmospheric noise surrounding this time, it cannot be discounted that it could be of random
547 origin.
548
549 This event was not detected using standard analysis, but extending a method that exploits
550 the ratios of the average energy residing between 2.4 Hz +/- 0.2 Hz, to different frequency bands
551 of the SP's and VBB's North, East and Vertical (Z) components. The algorithm was
552 implemented in steps of 0.4 Hz with 50% overlapping windows in frequency and avoiding
553 injection of tick noise (cross-talk noise generated by the SEIS temperature signal on the VBB
554 and SP seismic data). The resulting outliers were inspected against the average energy in the
555 Energy Short-Term Average (ESTA) channel (defined as the root mean square of data filtered
556 within a 0.5 second time window [Lognonné *et al.*, 2019]), to ensure they occurred during
557 calmer atmospheric periods, and to allow for further investigation.
558

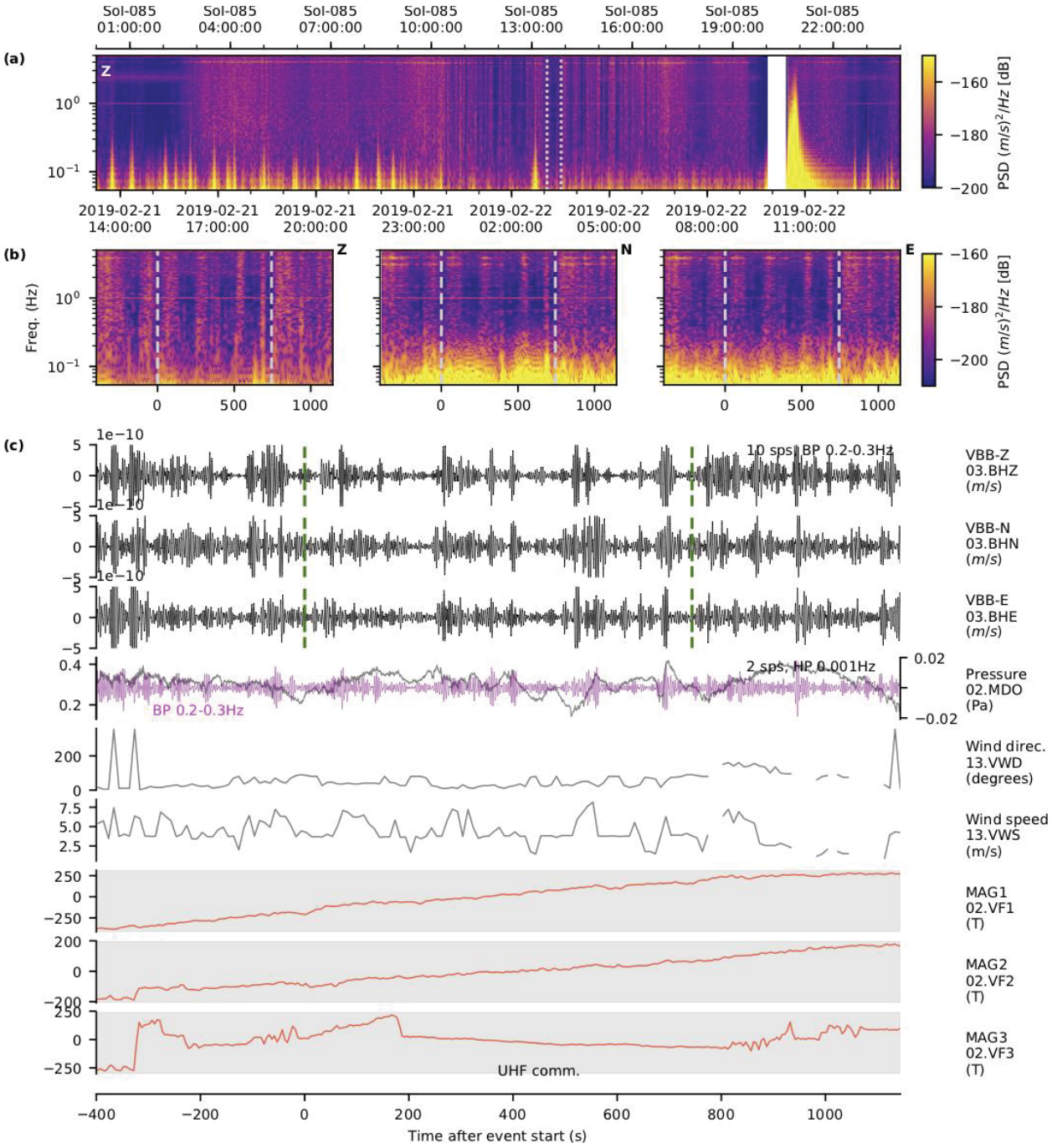

559

560 Figure 5.

561 *Summary of S0085a event. (a) provides the context of the event in the full sol spectrogram on the*
562 *VBB vertical (Z) component. (b) shows spectrograms for all 3 VBB components rotated into Z,*
563 *north (N) and east (E) orientations. The start and end time are indicted by the vertical dashed*
564 *white lines in (a) and (b). (c) shows timeseries from the 3 VBB velocity, pressure, wind direction,*
565 *wind speed, and 3 magnetometer channels. The data are filtered as indicated to accentuate*
566 *seismic and pressure signals. The vertical green dotted lines in (c) indicate the event start and*
567 *end times. In general in these summary figures, additional phase picks in green and glitch*

windows in red are overlain on the seismic channels; and on the magnetometer channels indications of any reported lander activity are shown in gray. For this event, however, the lander has UHF communications, there are no major glitches, and the event is too weak for MQS to identify phases. This event is extremely faint and not visible in the time series. The event is the very narrow band of energy at 0.7 Hz visible on the N component spectrogram. As explained in the text, this signal may not have a seismic source.

S0105a [2019/03/14 21:03:31, 18:07 LMST; MQS classification: Low Frequency, Quality C]

This Low Frequency event consists of two energy pulses, each without clear polarization (Fig. 6). It occurs around sunset, just after the transition from the high atmospheric situation of the day into the very quiet early evening. The amplitude of this event is so low that it could only have been reliably detected during ~25% of the time period of the impact. The total length of the signal is ~15 minutes, with at least 5 minutes uncertainty, given the relatively high noise level. The spectral energy is above the ambient noise between 0.3 and 0.5 Hz for the first pulse and 0.15 and 0.5 Hz for the second pulse. The spectrum of the two pulses is comparable to that of event S0173a, currently the largest LF event in the MQS catalog, but 16 dB lower at 0.3 Hz. The phases are emergent, and phase arrival picks for the two energy pulses cannot be made in the time domain, and so are made using a spectrogram and accordingly assigned high uncertainties of +/-20s. In the time domain, the separation of the two pulses is also similar to that of S0173a (160 seconds for S0105a vs 155 seconds for S0173a). The similarity of the signal of this event and other low frequency events is shown in Fig. 3 from Giardini *et al.*, 2020, and consistent with other larger events of this type, we assign P and S phases to the onset of these pulses. It would be difficult to convincingly assign these phase arrivals to P and S waves without the context of the wider seismicity so far recorded by InSight. Other interpretations may also be plausible, as discussed above in section 2.3, though this weak event is generally similar to stronger and more well-understood events.

Based on the time elapsed between these pulses, this event is estimated to be located at a distance of 27±5° (1600±300 km). For S0173a, a polarization analysis was also possible, resulting in a direction of the events as seen from the lander of 91±5°; thus it has been concluded this is the signal of a marsquake located in the Cerberus Fossae graben system (Giardini *et al.*, 2020). This fault system is the only place on Mars where more than one marsquake has been located so far, in agreement with pre-mission hypotheses of seismic activity there. A possible interpretation of the S0105a event is therefore that it is a smaller tectonic marsquake in a similar location to S0173a. As no polarization could be determined for S0105a, this interpretation must remain preliminary. The low signal-to-noise ratio also implies that no depth could be estimated for this or any other event in the impact time period.

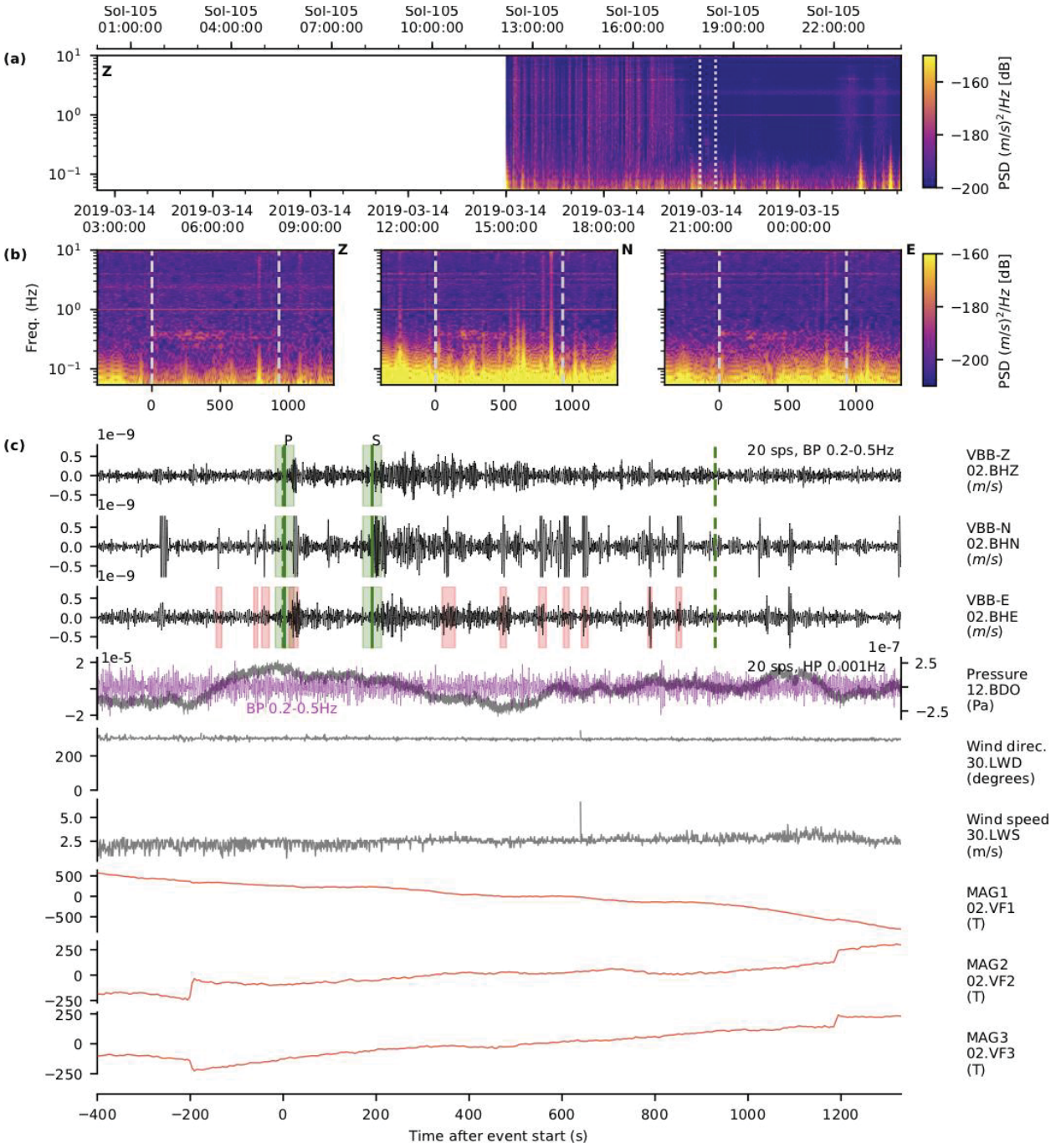

607

608 Figure 6.

609 *Summary of S0105a event, following Figure 5. During this event, there are multiple glitches (red*
610 *shaded windows), most clearly visible in the E component, and no lander activity. MQS also*
611 *identifies P and S phases (green solid vertical lines). Event energy is visible on all 3 components*
612 *in both time series and spectrograms.*
613

614 S0116a [2019/03/26 06:27:19 UTC, 20:11 LMST; MQS classification: High Frequency 2.4 Hz,
615 Quality D]
616
617 This High Frequency 2.4 Hz event, summarized in Figure 7, consists of an energy surplus
618 around the 2.4 Hz mode of about 7 dB in displacement power, concentrated into two pulses
619 separated by 78±10 seconds. At the time of detection, this event was unique, but as of the time of
620 writing, we have come to realize that it was just the first occurrence of a general class of similar
621 events, termed "2.4 Hz events". These are currently understood as being small High-Frequency
622 events. HF events are interpreted as shallow-source events occurring in a highly scattering layer
623 in the upper crust, probably shallower than the source region of the LF events. The absolute
624 distance of the HF events cannot be determined yet, as crustal seismic velocities are so far
625 unknown. The convention for these HF events is to label the start of each pulse as Pg and Sg
626 phases. From the separation of the two phases, a relative distance can be estimated. The S0116a
627 event is about four times closer than the majority of the HF events occurring later in the mission,
628 so it seems to have emanated from a difference source region. Only a handful of other events
629 share a similarly short Sg-Pg interval. Nevertheless, for it to have occurred at the detected impact
630 site, the shear wave velocity in the medium would have to be as low as 210 m/s (assuming a v_P/v_s
631 ratio of $\sqrt{3}$). Such a velocity is found in bedrock layers 5-10 m deep (Lognonné *et al.*, 2020), but
632 is unlikely at these shallow depths. In the MQS catalogue, all HF events are given an estimated
633 location using an assumed S wave velocity of v_s=2.3 km/s, and P wave velocity of $v_P=\sqrt{3}v_s$ =4.0
634 km/s. Using those assumed velocities, this event has an estimated distance of 11°, ~640 km from
635 the InSight lander. As the event is only visible as an excitation of the 2.4 Hz mode, its original
636 source spectrum cannot be constrained.
637
638 The amplitude of this event is so low that it could have been detected during only ~20%
639 of the day during the time period of the known impact.
640

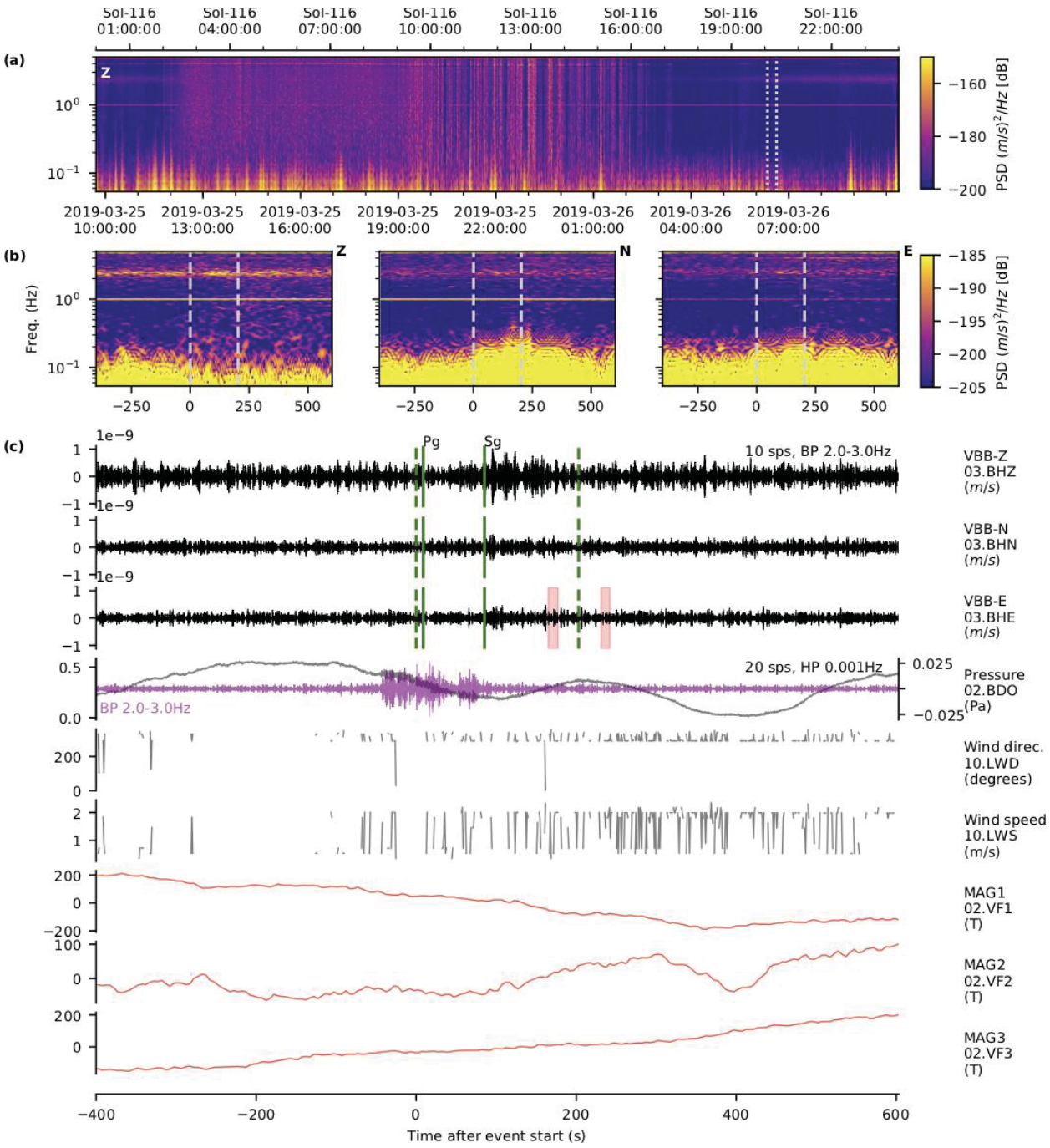

Figure 7.

Summary of S0116a event, following Figure 5. During this event, there are two minor glitches towards the end of the event (red shaded windows), and no lander activity. MQS also identifies tentative Pg and Sg phases (green vertical bars). Event energy at the 2.4 Hz resonance is weakly visible on all three components in both time series and spectrograms. An anomalous high frequency disturbance in the 2 sps pressure precedes the event, extending into the first minutes.

We note that nearly exactly 1 sol after the search period closed, the very high frequency event S0128a occurred. It can be seen in Figure 4, but outside the search period defined by the dashed white lines. This was one of the largest events so far recorded, and one of the events located closest to the InSight lander, although it is still estimated to be roughly ~8°±6° (~480 km ± 350 km) away (Giardini *et al.*, 2020, Lognonné *et al.*, 2020). Although the uncertainties on this distance estimate are large, they still do not encompass the small distance to this known impact. Additionally, the timing of the CTX images has been closely compared to this event timing, and the event does not fall within the possible time period for the new impact.

3.2 Evaluating seismic data for the candidate events

With regards to the three events detected within the search period, how can we evaluate which, if any, is the recording of the known image-constrained impact? Aside from their occurrence within the search period between 2/21/19 and 4/6/19, there are few other positive indicators that each of the signals was caused by the impact. Scaling relationships and analog comparisons predict the observed impact would create a seismic signal with peak energy ~a few Hz, with a peak amplitude of the P-wave ~0.8-4 nm/s. This range is also in good agreement with amplitudes from the numerical wave propagation simulations (supplemental section S2). However, none of the three candidate events includes energy above 2.4 Hz. The predicted duration of the event is ~30 seconds to one minute, although this is difficult to compare directly due to scattering. However, all candidate events have durations of over several minutes. We know the impact occurred at a backazimuth of 180.9°, so any polarization present in the signal should be in the north-south direction. S0105a and S0116a have no indication of polarization, though S0085a does include energy only in the N-S component, which is a match. Here we detail how well each of the candidate signals matches these expected characteristics (Table 2).

Table 2.

Expected characteristics of the seismic signal produced by the known impact, compared to the characteristics of each of the candidate seismic events. Matching characteristics are marked with a green check mark, non-matching characteristics are marked with a red "X", and neutral or undetected characteristics are marked with a black "~". Distance to source is measured from orbital images for the known impact and estimated for seismic events by MQS.

	Unambiguous seismic event?	**Amplitude (nm/s)**	**Peak Frequency (Hz)**	**Polarization**	**Duration (min)**	**Distance to source (km)**
Predicted for known impact:	***Uncertain***	***~0.8-4 nm/s***	***~2-3 Hz most likely for body waves***	***180.9° (approximately N/S)***	***30 sec - 1 minute***	***37.4 km (0.65°)***
S0085a	No,	0.3 nm/s	0.7 Hz	N/S	~10 min	Unknown

	very unusual signal occurring in noisiest time period ~	(North; Vertical and East not above noise) (bandpass 0.5-1 Hz, 6 pole) (approximately right) ✓	(too low) ✗	✓	Too long ✗	~
S0105a	Yes, clear LF event ~	1.5 nm/s (East), 0.5 nm/s (Vertical; North affected by glitches) (bandpass 0.2-0.67 Hz, 6 pole) (approximately right) ✓	0.15-0.5 Hz (too low) ✗	None identifiable ~	~15 min Too long ✗	1600±300 km (27±5°) ✗
S0116a	No, weak 2.4 Hz resonance ~	0.7 nm/s (Vertical) 0.5 nm/s (East) 0.5 nm/s (North) (bandpass 2.2-2.8 Hz, 6 pole) (approximately right) ✓	2.4 Hz (reasonable) ✓	None identifiable ~	~3 mins Too long ✗	Unknown ~

S0085a:

The event on sol 85 is the only one of the candidates with a measurable polarization, and it is in the correct direction relative to the impact. However, it is possible that this event may not be a seismic event at all – it could in fact be instrument-generated rather than a natural external source. Many spacecraft-induced signals will have a similar N/S polarization, as the InSight lander is towards the north of SEIS. Compared to other observed events, it has very narrow-band energy with an apparent dispersion, which is not expected for an impact. Even if this were a true seismic event, we cannot definitively identify it with the impact.

S0105a:

The event on sol 105, on the other hand, is a clear seismic event. Its amplitude (0.5 nm/s in the 0.2-0.67 Hz bandwidth on Vertical and 1.5 nm/s on East) is at the lower end of that predicted. The spectral peak is at a frequency lower than that predicted. If this is an impact at ~40 km, it would have to be explained why tens of other seismic events detected so far look very similar to this one. It is exceedingly unlikely that multiple small impacts occurred in this region in the same time period and we do not have any images of them; although we do not have complete repeat image coverage of the region out to ~40 km away from InSight in order to rule this out completely. Without definitive criteria for discriminating between impact and tectonic sources (see Section 4.1), we cannot exclude the possibility that one of these similar events is also an impact.

Figure 8 compares the S0105a signal with two Apollo impact records. All signals have been filtered with a 6th-order Butterworth bandpass (0.2-0.67 Hz), and SEIS data are expressed in Apollo Digital Units (DU). Amplitudes in Fig. 8 have been corrected with respect to distance using a -1.5 power law dependency with respect to the Apollo 14 LM impact recorded by the Apollo 14 LP seismometer, while the non-corrected amplitudes are given for each trace. The amplitude of the S0105 event is approximately 15 times smaller than that of the lunar LM impacts, which is within our estimate of a factor of 3.5-210 (see Section 2.3). The amplitude of the signal at 0.5 Hz can therefore be explained by the size of the known impact. However, neither the lack of high frequencies nor the duration of this event are compatible with what we expect for this impact.

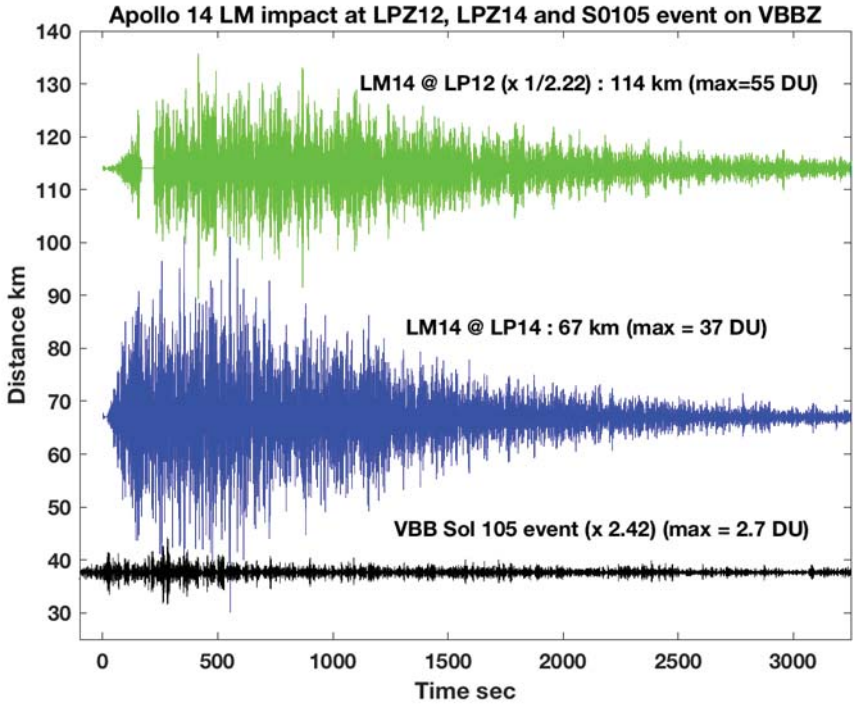

Figure 8.

Comparison between the martian event S0105a (black) and the Apollo 14 LM impact as recorded at two Apollo stations (green for Apollo 12 and blue for Apollo 14). The S0105a event has been deglitched (Lognonné et al., 2020) and converted into Apollo data units (DU) by using the Apollo Transfer function of the LP instruments. All events have been filtered with a 6^{th} order Butterworth bandpass between 0.2 and 0.67 Hz and corrected for the different distances by using a -1.5 power law with distance. Amplitude in DU as well as geometrical correction values are given on the figure. The very impulsive first arrival identified by MQS for S0105a is at time 0, followed by a second arrival 160 seconds later.

S0116a:

The event on sol 116 has an amplitude at the lower end of that predicted, though this is on top of the 2.4 Hz resonance, so is likely amplified. It has a higher frequency than the other events, which is reasonable for a small, local event. No polarization was detected, so no direction or distance can be estimated. In the months since this event was recognized, hundreds of other similar events have occurred, again making it unlikely this is due to an impact, which would occur relatively infrequently.

In summary, none of the three events can be unambiguously identified as the seismic signature of the new impact. The S0105a event can be explained as a relatively small tectonic marsquake in the Cerberus Fossae region. The S0116a could possibly be caused by the impact, but given its low amplitude, it cannot be further classified or analyzed. Both S0105a and S0116a are similar to numerous other events in the marsquake catalogue, suggesting they are not produced by a local impact signal, which we expect to be a rare occurrence. The S0085a signal is extremely weak, and its very narrow-band nature suggests it is not likely to have been caused by an external seismic event.

We note the extreme variation in diurnal noise means that significantly larger events than the three identified here may be hidden in the data. As noted, the amplitude we predict for this impact is quite close to the measured noise levels of SEIS during the least noisy time periods (Fig. 4). Given daily and seasonal variations in temperature and wind activity, the noise levels are lowest in the evening (Lognonné *et al.*, 2020; Fig. 4). Signals on the order of the predicted amplitude would only be observable (at ~3 SNR) for ~20-30% of the time. Thus, the actual signal from this impact could very likely have occurred at a time when noise swamped the signal.

Another observational bias could occur due to the 2.4 Hz signals. These are a resonance seen in numerous other events (Giardini *et al.*, 2020), and this is also near the peak frequency expected for impact event. Such a resonance could enhance smaller signals, allowing detection of signals that are otherwise ~ten times smaller if they are near the resonance. This might help our detection likelihood, but it is also a narrow band, making source discrimination more difficult.

3.3 Evaluating atmospheric data for the candidate events

Although no obvious atmospheric signals were associated with the three seismic candidates, each event was investigated to eliminate that possibility:

S0085a occurred in the local early afternoon (unlike the S0105a and S0116a events). Atmospheric variability for S0085a is thus mostly governed by convective turbulence (cells and vortices), usually found in daytime hours. There were no vortex signals close to the event that might have affected the seismic signal. Under normal conditions, gravity waves are not usually detected in daytime hours, based on the first 300 sols of InSight measurements (Banfield *et al.*, 2020), and no gravity waves were detected around the time of this event.

There was no notable atmospheric signal associated directly with the S0105a event. Pressure and temperature measurements were uneventful, and the wind was steady and low. Two hours after the seismic event, a gravity wave of strong amplitude (+/- 0.5 Pa) with a period of 400-600 seconds was detected. However, between sols 100-150, similar signals were very frequently seen at these local times (~20:00 LMST). Furthermore, given the proximity of the impact to InSight, a propagation speed that would cause a two hour delay between the seismic signal and the atmospheric wave packet is far too low to be realistic. This is based on typical gravity wave phase speeds estimated by Banfield *et al.* (2020) of ~20-30 m/s. The gravity wave signal reached InSight two hours after the seismic event; even accounting for background wind, the gravity wave would be too fast to have been emitted by the atmospheric entry of a meteoroid at 37.4 km distance. It is thus not likely to be related to the seismic event.

For S0116a, a gravity wave signal was found in the pressure signal at a time near the seismic event. However, it started about a quarter of an hour before the seismic signal, which implies the two are unrelated. Wind and temperature measurements behaved as usual for evening conditions at the InSight landing site. Interestingly, around the start of the event, just before the seismic signal, the pressure signal also underwent high-frequency fluctuations in the infrasonic range (*i.e.* <20 Hz). Though an impulsive pressure signal could be expected from a close impact event, the long duration HF pressure wave packet we observed is similar to scattered pressure signals related to explosions seen in infrasound records on Earth (Green *et al.*, 2011). Such scatterings of acoustic energy can occur when small-scale gravity waves perturb the lower atmosphere wave guide (e. g. Green *et al.*, 2011; Damiens *et al.*, 2017). Nonetheless, other facts concur to put aside the impact hypothesis as a source of the observed pressure fluctuations: (1) high-frequency pressure fluctuations are recorded by InSight almost every sol in the evening, (Banfield *et al.*, 2020), (2) acoustic propagation models (Garcia *et al.*, 2017; Spiga *et al.*, 2018) show that the InSight lander is in a shadow zone for infrasound waves generated at the impact location (Fig. S11) and (3) owing to the noise levels of the respective instruments, if infrasound signals were seen in InSight pressure data, they would also be seen in the seismic data. They would also have to be at a significantly larger distance than this case (Martire *et al.*, 2020). This makes it very difficult to ascribe these particular pressure fluctuations to the sol 116 seismic event, or to any impact-induced phenomena at the distance of the known impact.

Regarding an airburst signal, none of the candidate events have two distinct arrivals with the expected temporal spacing of ~2 minutes (Section 2.4), even if they were above the detection

808 threshold. So we do not believe an impact airburst was detected for this event. To summarize,
809 while interesting atmospheric signals were noticed during the three events, they are not likely
810 related to either the seismic events in question or to the impact event.
811

812 **4 Discussion**

813 4.1 Re-assessment of seismic impact discriminators

814
815 Over the first months of the InSight mission, we have learned that marsquakes (whether
816 sources are impact or tectonic) differ from our previous experience with either terrestrial or lunar
817 analogs. The impact discriminators we planned on using before arriving at Mars (Daubar *et al.*,
818 2018) have limited utility given the reality of martian seismic signals recorded thus far. The
819 marsquakes observed so far are small in amplitude, with surprisingly long durations, and with
820 apparently low attenuation / high Q. This makes many of these characteristics difficult to
821 distinguish. We re-assess (*in italics*) each of those planned discriminators in light of real seismic
822 data from InSight:
823
824 1) First motion: Impacts create positive pressure impulses, creating a positive first motion,
825 in a direction away from the source.
826 ▪ *Despite the low noise recorded by InSight during periods of the day, marsquake*
827 *signals have proven to be very small. In all but the largest signals seen so far,*
828 *phase arrivals are emergent, so noise obscures the direction of first arrivals.*
829 *Scattering in the regolith randomizes the energy.*
830 ▪ *Even if we had clear first motions, quakes with a double couple source would*
831 *have a positive first motion 50% of the time anyway, assuming a random*
832 *orientation of sources.*
833 2) S-wave energy: Impacts produce more P-waves than S-waves.
834 ▪ *A quake could also have low S energy for an unfavorable source orientation.*
835 ▪ *S-waves are obscured by scattered P energy, so this is hard to determine for small*
836 *events.*
837 3) Magnitude ratio: Impacts produce fewer surface waves, so impacts should have a strong
838 difference between magnitudes based on body waves and those based on surface waves.
839 ▪ *Surface waves are not being detected for any martian events (Giardini et al.,*
840 *2020). The absence or diminished presence of surface wave energy, therefore,*
841 *cannot be used as an impact discriminator, because all events lack surface waves.*
842 4) Frequency content: Different source mechanisms lead to a smaller cutoff frequency for
843 impacts.
844 ▪ *Cutoff frequencies for the largest of the detected martian events, where they can*
845 *be determined, are typically near 6 Hz but can rise up to 12 Hz (Giardini et al.,*
846 *2020). This cutoff frequency is much higher than the ~1-3 Hz expected for impacts*
847 *(Daubar et al., 2018).*
848 5) Depth phases: Impacts occur at the surface, implying no depth reflected phases.
849 ▪ *Additional phases beyond P and S arrivals have not been identified in any events*
850 *thus far (Giardini et al., 2020) because of scattering and the resulting extended*
851 *codas, so a lack of depth phases cannot be used to indicate an impact.*

852

853 4.2 Revised predictions of impact detections by InSight

854

855 As this is the only impact known to have occurred this close to InSight during its prime
856 science monitoring phase thus far, we wish to evaluate how likely this particular impact event
857 was. Using an estimated current cratering rate, we can estimate the probability of a ~1 m
858 diameter crater forming within ~50 km of InSight in one Earth year. Unfortunately, the cratering
859 rate for impacts of this scale is not well constrained. As an estimate, we use a production
860 function based on an extrapolation of the fragmentation model of Williams *et al.* (2014) pinned
861 to the production function based on observed dated craters from Daubar *et al.* (2013) (see
862 Teanby 2015 for more details). The resulting rate is ~2×10^{-5} impacts >1 m diameter/km^2/Earth
863 year. The uncertainty on this value is probably at least a factor of 10 in both directions. For this
864 impact rate, the probability of one impact in any given circle of radius 50 km each Earth year is
865 ~0.2. Thus this event is not completely unlikely, but we were quite lucky to catch it in the
866 images, which have covered only a small fraction of that area multiple times since Insight
867 landed.
868
869 Based on measured noise levels of SEIS on the ground at Mars, we can revise our pre-
870 landing estimates of the number and size of impact detections to expect during the InSight
871 mission. Teanby and Wookey (2011) and Teanby (2015) estimated seismic impact detection
872 rates with predicted Mars seismic noise. We can now update these predictions using measured
873 noise levels from the first few months of InSight operations. Teanby and Wookey (2011) model
874 results for large impacts predict their peak seismic energy will be in the 1-2 Hz frequency range
875 (where the SEIS-VBB instrument is most sensitive). Teanby (2015) compiled observations from
876 small impacts and explosions to suggest that their peak seismic energy will be in the 1-8 Hz
877 frequency range (where the SEIS-SP instrument is most sensitive). Typical SEIS noise levels are
878 0.3-10 x 10^{-9} m/s^2/Hz$^{1/2}$ in the 1-8 Hz range (Lognonné *et al.*, 2020), although during much of the
879 martian day SEIS sees considerably higher noise than these levels. Using scaling relationships
880 developed in previous work (Teanby, 2015; Teanby and Wookey 2011), we can predict P-wave
881 amplitudes for different size impacts at various distances (Fig. 2). To get the expected frequency
882 of impacts of different sizes, we use the production function developed by Teanby (2015) that
883 uses new dated craters from Daubar *et al.* (2013) extrapolated to smaller diameters to account for
884 the observational rollover using the Williams *et al.* (2014) fragmentation model. As signals at the
885 noise level are very difficult to detect (as demonstrated by this paper!), we use a more
886 conservative restriction of SNR~3 to be realistic. InSight's noise measurements show that the
887 martian day can be roughly split into low-noise and high-noise time periods. Assuming a typical
888 low noise level of 1.5 x 10^{-9} m/s^2/Hz$^{1/2}$ at 4 Hz (Lognonné *et al.*, 2020) is appropriate
889 approximately 50% of the time, and the remaining 50% of the time it is too noisy for any
890 detections, we predict just ~2 detections of impact events per Earth year, during times when
891 higher continuous rate data are collected. Furthermore, seismic amplitudes of signals from small
892 craters could be even lower (Wójcicka *et al.*, 2020) resulting in even fewer detections. There are
893 still large uncertainties on the predicted detection rate, at least an order of magnitude. However,
894 given that we have yet to unambiguously detect any impacts in the seismic data, either the large
895 end of this range is increasingly unlikely, or – more likely – we have not yet learned enough
896 about martian seismic signals to recognize impacts in the data.

Because of this revised expectation of seismic detections of impacts, we have reversed our operational approach to detecting impacts. Instead of examining the seismic data for possible impact-induced signals, then following up with orbital images appropriate for the expected size and location of the impact, as described in Daubar *et al.* (2018), we are instead examining orbital images for new impacts, as indicated by dark spots or albedo changes near InSight. When more of these are found, we will examine the seismic data during the image-constrained time periods in a manner similar to the analysis presented here.

5 Conclusions

The exciting and lucky observation of a new impact occurring very close to the InSight lander during its prime mission presented a first opportunity to test our understanding of the seismic detectability of small impacts on Mars. Three potential candidate events were identified in the seismic data during the time period constrained by the before and after orbital CTX images; however, we are not able to determine that any of those seismic or atmospheric signals were definitively associated with that impact event. This is mainly because although the impact was nearby, it was quite small, forming only a ~1.5 m diameter crater, and likely was created by a significantly decelerated impactor. We predict that the signals produced by this impact were very close to the measured minimum noise amplitudes seen by the InSight seismometers, and for a good portion of the time, the observed noise levels are well above the predicted impact signal amplitude. Thus a lack of detection for an impact of this size and at this location is disappointing, but not surprising.

There are many uncertainties in our predictions of seismic signals from the known impact, for example in converting crater size to seismic moment. The attenuation and scattering properties of the martian crust are not yet completely understood, nor is the velocity structure of the subsurface. Given the uncertainties in our predictions, it is still possible that the known crater was indeed responsible for one of the three candidate seismic events, although we cannot support that conclusion with our current knowledge. As InSight reveals more about the properties of the martian interior, the uncertainties in our predictions will be reduced. Future efforts at numerical modeling of this specific impact and coupled seismic modeling of the resulting wave propagation may reveal additional things to look for in the seismic or atmospheric data that may allow us to identify future impacts, if not this particular event. As we did not positively detect this impact in the data, we can at least conclude that we are not grossly underestimating the seismic amplitudes from impact events. Likewise, we see no definitive signals associated with this impact in the atmospheric data, nor do we expect that would be likely in this specific case.

The process of searching within the continuous seismic data from InSight for evidence of an event associated with an image-constrained impact has refined our understanding of impact-generated seismic signals through forward modelling and allowed us to reevaluate our predictions of impact detectability. Using the now-known noise levels of the SEIS instrument on

Mars, we expect ~2 impact detections with SNR>3 each Earth year. This is assuming continued high sampling rates able to detect higher frequency peaks, which have lately begun. Our continued efforts to search orbital images for new dated impacts near InSight will almost certainly result in more image-constrained impacts. This work has provided a template workflow to help us quickly identify future impact seismic signals associated with image-detected craters. We continue to listen for impacts on Mars.

Acknowledgements

We thank the CTX and HiRISE operations teams for the initial identification of the site, and careful and timely acquisition of the images used to make this discovery. We acknowledge NASA, CNES, their partner agencies and Institutions (UKSA, SSO, DLR, JPL, IPGP-CNRS, ETHZ, IC, MPS-MPG) and the flight operations team at JPL, SISMOC, MSDS, IRIS-DMC and PDS for acquiring and providing InSight data, including SEED SEIS data. We thank two anonymous reviewers for their constructive input.

IJD is supported by NASA InSight Participating Scientist grant 80NM0018F0612. NAT, JW & AH are supported by UK Space Agency grant ST/R002096/1. The French Team acknowledge the French Space Agency CNES and ANR (ANR-14-CE36-0012-02, ANR-19-CE31-0008-08). The Swiss co-authors were jointly funded by (1) Swiss National Science Foundation and French Agence Nationale de la Recherche (SNF-ANR project 157133 “Seismology on Mars”), (2) Swiss State Secretariat for Education, Research and Innovation (SEFRI project “MarsQuake Service-Preparatory Phase”) and (3) ETH Research grant ETH-06 17-02. GSC & NW are supported by STFC grants ST/S000615/1, ST/S001514/1. KM and AR are fully supported by the Australian Research Council (DP180100661 and DE180100584). A part of the 3-D simulations in the supplementary material was performed on the Earth Simulator of the Japan Agency for Marine-Earth Science and Technology (JAMSTEC), another part on resources provided by the Los Alamos National Laboratory Computing Program supported by DOE. A portion of this research was carried out at the Jet Propulsion Laboratory, California Institute of Technology, under a contract with the National Aeronautics and Space Administration. This is InSight contribution number 104 and IPGP contribution XXX.

All data used in this work are publicly available via the Planetary Data System (PDS; https://pds.nasa.gov/). Specifically, CTX images can be found at https://pds-imaging.jpl.nasa.gov/volumes/mro.html, HiRISE images can be found at https://www.uahirise.org/, and InSight APSS/TWINS/PS data can be found at https://atmos.nmsu.edu/data_and_services/atmospheres_data/INSIGHT/insight.html. InSight SEIS data is available in the form of a seismic event catalogue (DOI: 10.12686/a6) and waveform data (DOI: 10.18715/SEIS.INSIGHT.XB_2016) that are publicly available from the IPGP Datacenter and IRIS-DMC, as well as raw data available in the PDS at https://pds-geosciences.wustl.edu/missions/insight/seis.htm. Apollo seismic data are available in raw form at https://darts.isas.jaxa.jp/planet/seismology/apollo/index.html, and the data are available in SEED format from the IPGP Data Center for lunar data (Code XA, http://datacenter.ipgp.fr/data.php).

Seismic modeling results and parameters are available on the IPGP data center at https://doi.10.18715/JGR_NewCraterMod_2020.

References

Banfield, D. *et al. (*2020) First results from InSight's meteorology station on Mars. Nature Geoscience, 13, pp. 190-198. DOI: 10.1038/s41561-020-0534-0

Clinton, J., Giardini, D., Böse, M., S. Ceylan, M. van Driel, F. Euchner, R. F. Garcia, S. Kedar, A. Khan, S. C. Stähler, B. Banerdt, P. Lognonné, E. Beucler, I. Daubar, M. Drilleau, M. Golombek, T. Kawamura, M. Knapmeyer, B. Knapmeyer-Endrun, D. Mimoun, A. Mocquet, M. Panning, C. Perrin, N. A. Teanby, The Marsquake Service: Securing Daily Analysis of SEIS Data and Building the Martian Seismicity Catalogue for InSight, Space Sci Rev (2018) 214: 133. https://doi.org/10.1007/s11214-018-0567-5

Damiens, F., C. Millet, and F. Lott, 2017: An investigation of infrasound propagation over mountain ranges, Journal of the Acoustical Society of America, 2018, 143:1, 563-574

Daubar, I. J., McEwen, A. S., Byrne, S., Kennedy, M. R., Ivanov, B., 2013. The current martian cratering rate. Icarus 225, 506–516.

Daubar, I., Lognonné, P., Teanby, N.A., Miljkovic, K., Stevanović, J., Vaubaillon, J., Kenda, B., Kawamura, T., Clinton, J., Lucas, A., Drilleau, M., Yana, C., Collins, G.S., Banfield, D., Golombek, M., Kedar, S., Schmerr, N., Garcia, R., Rodriguez, S., Gudkova, T., May, S., Banks, M., Maki, J., Sansom, E., Karakostas, F., Panning, M., Fuji, N., Wookey, J., van Driel, M., Lemmon, M., Ansan, V., Böse, M., Stähler, S., Kanamori, H., Richardson, J., Smrekar, S., Banerdt, W.B., 2018. Impact-Seismic Investigations of the InSight Mission. Space Sci Rev 214, 132. https://doi.org/10.1007/s11214-018-0562-x

Daubar, Ingrid Justine, M. E. Banks, N. C. Schmerr, and Matthew P. Golombek. 2019. "Recently Formed Crater Clusters on Mars." *Journal of Geophysical Research: Planets*. https://doi.org/10.1029/2018JE005857.

Garcia, Raphaël F., Quentin Brissaud, Lucie Rolland, Roland Martin, Dimitri Komatitsch, Aymeric Spiga, Philippe Lognonné, and William Bruce Banerdt. 2017. "Finite-Difference Modeling of Acoustic and Gravity Wave Propagation in Mars Atmosphere: Application to Infrasounds Emitted by Meteor Impacts." *Space Science Reviews* 211 (1–4): 547–70. https://doi.org/10.1007/s11214-016-0324-6.

Giardini, D., Lognonné, P., Banerdt, W.B. et al. The seismicity of Mars. Nat. Geosci. 13, 205–212 (2020). https://doi.org/10.1038/s41561-020-0539-8

Gillet, K., L. Margerin, M. Calvet, and M. Monnereau (2017) Scattering attenuation profile of the Moon: Implications for shallow moonquakes and the structure of the megaregolith. Physics of the Earth and Planetary Interiors 262, 28-40. DOI:10.1016/j.pepi.2016.11.001

Golombek, M. P. *et al. (*2020) "Geology of the InSight Landing Site on Mars." Nature Communications, 11, 1014. https://doi.org/10.1038/s41467-020-14679-1.

1026 Green, D. N., Julien Vergoz, Robert Gibson, Alexis Le Pichon, Lars Ceranna. (2011) Infrasound
1027 radiated by the Gerdec and Chelopechene explosions: propagation along unexpected
1028 paths, *Geophysical Journal International*, Volume 185, Issue 2, Pages 890–910,
1029 https://doi.org/10.1111/j.1365-246X.2011.04975.x

1030 Gudkova, T., Lognonné, P. , Gagnepain-Beyneix, J., 2011. Seismic source inversion for Large
1031 impacts detected by the Apollo seismometers, *Icarus*, **211**, 1049-1065, doi :
1032 10.1016/j.icarus.2010.10.028.

1033 Gudkova, Tamara V., Philippe Lognonné, Katarina Miljković, and Jeannine Gagnepain-Beyneix.
1034 2015. "Impact Cutoff Frequency – Momentum Scaling Law Inverted from Apollo
1035 Seismic Data." *Earth and Planetary Science Letters* 427: 57–65.
1036 https://doi.org/10.1016/j.epsl.2015.06.037.

1037 Holsapple, K.A., 1993. The scaling of impact processes in planetary sciences. Ann. Rev. Earth
1038 Planet. Sci. 21, 333–373. https://doi.org/10.1146/annurev.ea.21.050193.002001

1039 Holsapple, K.A., Housen, K.R., 2007. A crater and its ejecta: An interpretation of Deep Impact.
1040 Icarus 187, 345--356. https://doi.org/10.1016/j.icarus.2006.08.029

1041 InSight Mars SEIS data Service (2019) SEIS raw data, InSight Mission. IPGP, JPL, CNES,
1042 ETHZ, ICL, MPS, ISAE-Supaero, LPG, MSFC. Other/Seismic Network,
1043 https://doi.org/10.18715/SEIS.INSIGHT.XB_2016

1044 InSight Marsquake Service (2020) Mars Seismic Catalogue, InSight Mission; V1 2/1/2020.
1045 ETHZ, IPGP, JPL, ICL, ISAE-Supaero, MPS, Univ Bristol. Dataset.
1046 http://doi.org/10.12686/a6

1047 JeongAhn, Youngmin, and Renu Malhotra. 2015. "The Current Impact Flux on Mars and Its
1048 Seasonal Variation." *Icarus* 262: 140–53. https://doi.org/10.1016/j.icarus.2015.08.032.

1049 Karakostas, Foivos, Virgile Rakoto, Philippe Lognonné, Carene Larmat, Ingrid Justine Daubar,
1050 and Katarina Miljković. 2018. "Inversion of Meteor Rayleigh Waves on Earth and
1051 Modeling of Air Coupled Rayleigh Waves on Mars." *Space Science Reviews* 214 (8):
1052 127. https://doi.org/10.1007/s11214-018-0566-6.

1053 Komatitsch, D. and Tromp, J., 2002. Spectral-element simulations of global seismic wave
1054 propagation—I. Validation. Geophysical Journal International, 149(2), pp.390-412.

1055 Leng, K., Nissen-Meyer, T. and van Driel, M., 2016. Efficient global wave propagation adapted
1056 to 3-D structural complexity: a pseudospectral/spectral-element approach. Geophysical
1057 Supplements to the Monthly Notices of the Royal Astronomical Society, 207(3),
1058 pp.1700-1721.

1059 Le Feuvre, M, and Mark A. Wieczorek. 2008. "Nonuniform Cratering of the Terrestrial Planets."
1060 *Icarus* 197 (1): 291–306. https://doi.org/10.1016/j.icarus.2008.04.011.

1061 Lesage, P., M. J. Heap, and A. Kushnir (2018) A generic model for the shallow velocity structure
1062 of volcanoes. Journal of Volcanology and Geothermal Research 356, 114-126.
1063 DOI:10.1016/j.jvolgeores.2018.03.003

1064 Lognonné, P., Banerdt, W.B., Pike, W.T. et al. Constraints on the shallow elastic and anelastic
1065 structure of Mars from InSight seismic data. Nat. Geosci. 13, 213–220 (2020).
1066 https://doi.org/10.1038/s41561-020-0536-y

1067 Lognonné, P., Banerdt, W.B., Giardini, D. *et al.*, SEIS: Insight's Seismic Experiment for
1068 Internal Structure of Mars, Space Sci Rev (2019) 215: 12.
1069 https://doi.org/10.1007/s11214-018-0574-6

1070 Lognonné, P., Karakostas, F., Rolland, L. and Nishikawa, Y., 2016. Modeling of atmospheric-
1071 coupled Rayleigh waves on planets with atmosphere: From Earth observation to Mars
1072 and Venus perspectives. The Journal of the Acoustical Society of America, 140(2),
1073 pp.1447-1468.

1074 Lognonné, P., M. Le Feuvre, C. L. Johnson, and R. C. Weber (2009), Moon meteoritic seismic
1075 hum: steady state prediction, *J. Geophys. Res.*, **114**, E12003, doi:10.1029/2008JE003294.

1076 Maeda, T., Takemura, S. and Furumura, T., 2017. OpenSWPC: an open-source integrated
1077 parallel simulation code for modeling seismic wave propagation in 3D heterogeneous
1078 viscoelastic media. Earth, Planets and Space, 69(1), p.102.

1079 Malin, Michael C., James F. Bell, Bruce A. Cantor, Michael a. Caplinger, Wendy M. Calvin, R.
1080 Todd Clancy, Kenneth S. Edgett, *et al.,* 2007. "Context Camera Investigation on Board
1081 the Mars Reconnaissance Orbiter." *Journal of Geophysical Research* 112 (E5): E05S04.
1082 https://doi.org/10.1029/2006JE002808.

1083 Martire L., R. Garcia, L. Rolland, A. Spiga, P. Lognonné, D. Banfield,
1084 W. B. Banerdt, R. Martin (2020) Martian Infrasound: Numerical Modeling and Analysis
1085 of InSight's Data. Journal of Geophysical Research (Planets), submitted.

1086 McEwen, Alfred S., Eric M. Eliason, James W. Bergstrom, Nathan T. Bridges, Candice J.
1087 Hansen, W. Alan Delamere, John a. Grant, *et al.,* 2007. "Mars Reconnaissance Orbiter's
1088 High Resolution Imaging Science Experiment (HiRISE)." *Journal of Geophysical*
1089 *Research* 112 (E5): E05S02. https://doi.org/10.1029/2005JE002605.

1090 McMullan, S. and G. S. Collins (2019) Uncertainty quantification in continuous fragmentation
1091 airburst models. Icarus 327, 19-35. DOI:10.1016/j.icarus.2019.02.013

1092 Moore, H. J. (1976) Missile impact craters (WSPR, New Mexico) and applications to lunar
1093 research, Geological Survey Professional Paper 812-B, (contributions to Astrogeology).

1094 Nissen-Meyer, T., Driel, M.V., Stähler, S., Hosseini, K., Hempel, S., Auer, L., Colombi, A. and
1095 Fournier, A., 2014. AxiSEM: broadband 3-D seismic wavefields in axisymmetric media.
1096 Solid Earth, (1), pp.425-445.

1097 Parker, Timothy J., Matthew P. Golombek, F. J. Calef, N. R. Williams, S. LeMaistre, W.
1098 Folkner, Ingrid Justine Daubar, *et al.,* 2019. "Localization of the InSight Lander." *50th*
1099 *Lunar and Planetary Science Conference, Held 18-22 March, 2019 at The Woodlands,*
1100 *Texas. LPI Contribution No. 2132, Id.1948* 50.
1101 http://adsabs.harvard.edu/abs/2019LPI....50.1948P.

1102 Plescia, J.B., Robinson, M.S., Wagner, R., Baldridge, R., 2016. Ranger and Apollo S-IVB
1103 spacecraft impact craters. Planetary and Space Science 124, 15–35.
1104 https://doi.org/10.1016/j.pss.2016.01.002

1105 Revelle, D.O., P.G. Brown, P. Spurny, Entry dynamics and acoustics/infrasonic/seismic analysis
1106 for the ` Neuschwanstein meteorite fall. Meteorit. Planet. Sci. 39(10), 1605–1626 (2004)

1107 Rivoldini, A., Van Hoolst, T., Verhoeven, O., Mocquet, A. and Dehant, V., 2011. Geodesy
1108 constraints on the interior structure and composition of Mars. Icarus, 213(2), pp.451-472.

1109 Sato, H. and M. Korn (2007) Envelope syntheses of cylindrical vector-waves in 2-D random
1110 elastic media based on the Markov approximation. Earth, Planets, and Space 59, 209-219.

1111 Schmerr, N. C., M. Banks, and Ingrid Justine Daubar. 2019. "The Seismic Signatures of
1112 Recently Formed Impact Craters on Mars." *Journal of Geophysical Research: Planets*,
1113 1–19. https://doi.org/10.1029/2019je006044.

1114 Schmidt, R.M., Housen, K.R., 1987. Some recent advances in the scaling of impact and
1115 explosion cratering. International Journal of Impact Engineering, Hypervelocity Impact
1116 Proceedings of the 1986 Symposium 5, 543–560. https://doi.org/10.1016/0734-
1117 743X(87)90069-8

1118 Shishkin, N.I., 2007. Seismic efficiency of a contact explosion and a high-velocity impact. J.
1119 Appl. Mech. Tech. Phys. 48, 145–152. https://doi.org/10.1007/s10808-007-0019-6

1120 Smrekar, Suzanne E., Philippe Lognonné, Tilman Spohn, W. Bruce Banerdt, Doris Breuer,
1121 Ulrich Christensen, Véronique Dehant, *et al.,* 2019. "Pre-Mission InSights on the Interior
1122 of Mars." *Space Science Reviews* 215 (1): 3. https://doi.org/10.1007/s11214-018-0563-9.

1123 Spiga, Aymeric, Don Banfield, Nicholas A. Teanby, François Forget, Antoine Lucas, Balthasar
1124 Kenda, Jose Antonio Rodriguez Manfredi, *et al.,* 2018. "Atmospheric Science with
1125 InSight." *Space Science Reviews*. Springer Netherlands. https://doi.org/10.1007/s11214-
1126 018-0543-0.

1127 Stevanović, J., Teanby, N.A., Wookey, J., Selby, N., Daubar, I.J., Vaubaillon, J. and Garcia, R.,
1128 2017. Bolide airbursts as a seismic source for the 2018 Mars InSight mission. Space
1129 Science Reviews, 211(1-4), pp.525-545.

1130 Teanby, N. A., 2015. Predicted detection rates of regional-scale meteorite impacts on Mars with
1131 the InSight short-period seismometer. Icarus 256, 49–62.

1132 Teanby, N.A., Wookey, J., 2011. Seismic detection of meteorite impacts on Mars. Physics of the
1133 Earth and Planetary Interiors 186, 70–80. https://doi.org/10.1016/j.pepi.2011.03.004

1134 Williams, J.P., Pathare, A.V., Aharonson, O., 2014. The production of small primary craters on
1135 Mars and the Moon. Icarus 235, 23–36.

1136 Wójcicka, N., Collins, G.S., Bastow, I.D., Teanby, N.A., Miljković, K., Rajšić, A., Daubar, I.,
1137 Lognonné, P., 2020. The seismic moment and seismic efficiency of small1impacts on
1138 Mars. JGR Planets, submitted this issue.

1139

Figure 1.

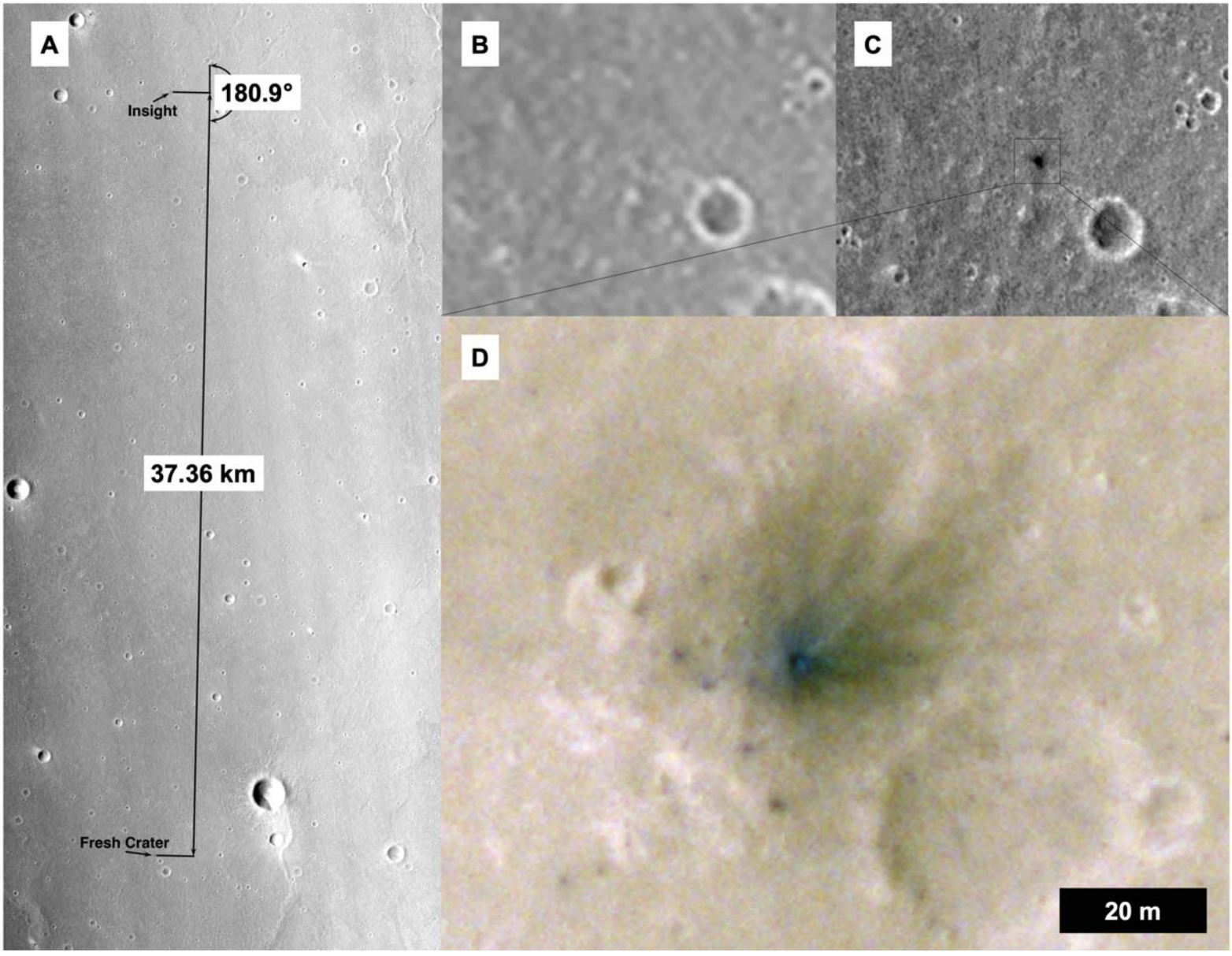
A
Insight
180.9°
37.36 km
Fresh Crater
B
C
D
20 m

Figure 2.

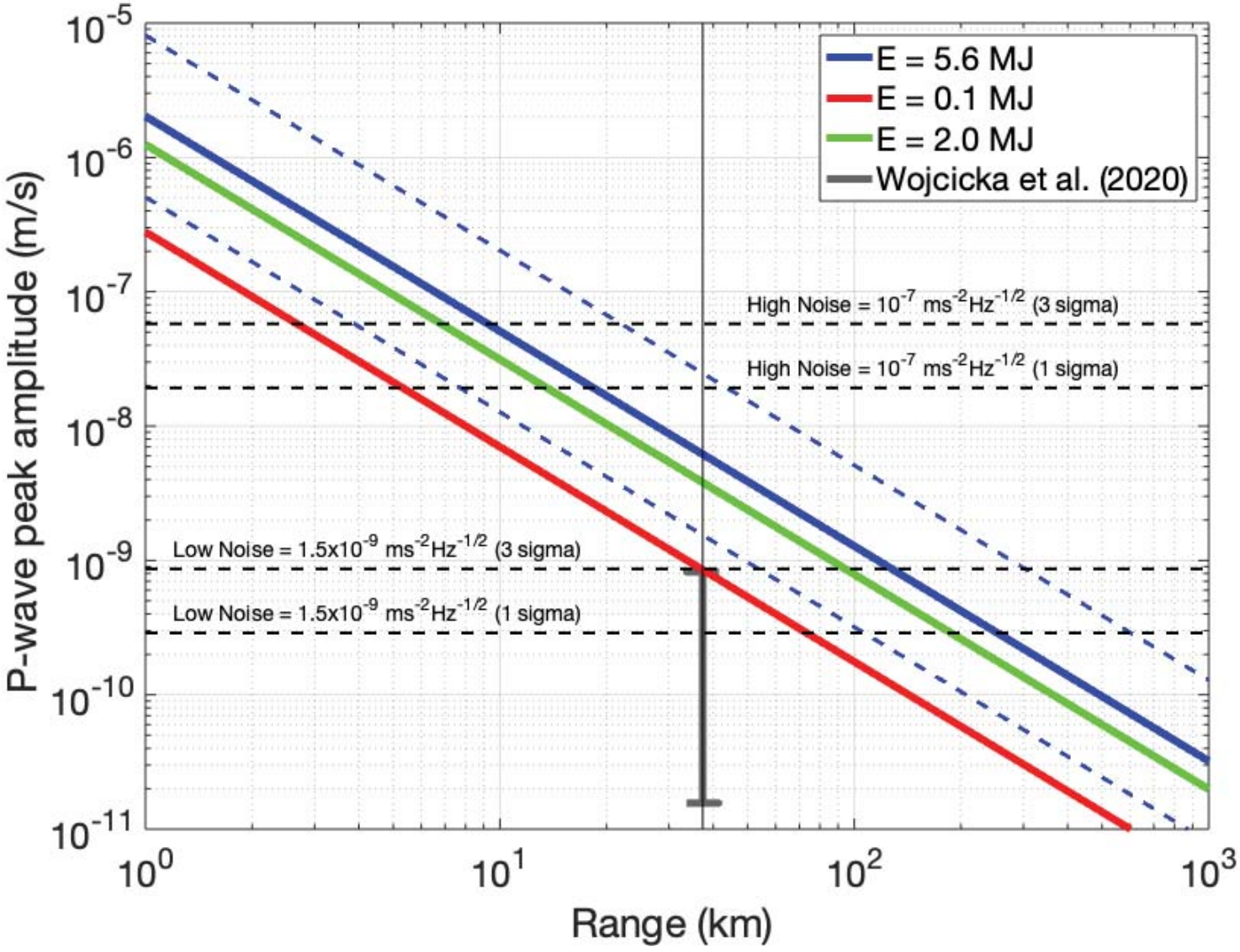
E = 5.6 MJ
E = 0.1 MJ
E = 2.0 MJ
Wojcicka et al. (2020)
High Noise = 10^-7 ms^-2Hz^-1/2 (3 sigma)
High Noise = 10^-7 ms^-2Hz^-1/2 (1 sigma)
Low Noise = 1.5x10^-9 ms^-2Hz^-1/2 (3 sigma)
Low Noise = 1.5x10^-9 ms^-2Hz^-1/2 (1 sigma)
P-wave peak amplitude (m/s)
Range (km)
10^-5
10^-6
10^-7
10^-8
10^-9
10^-10
10^-11
10^0
10^1
10^2
10^3

Figure 3.

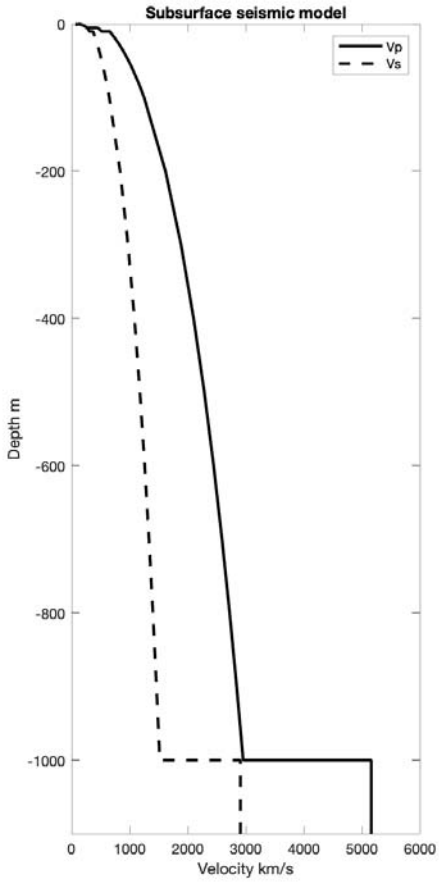
Subsurface seismic model
Vp
Vs
Depth m
0
-200
-400
-600
-800
-1000
0
1000
2000
3000
4000
5000
6000
Velocity km/s

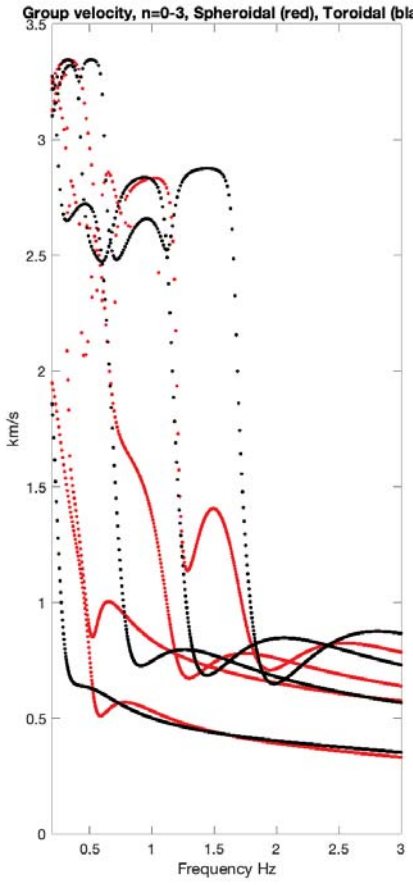
Group velocity, n=0-3, Spheroidal (red), Toroidal (blak)
km/s
3.5
3
2.5
2
1.5
1
0.5
0
0.5
1
1.5
2
2.5
3
Frequency Hz

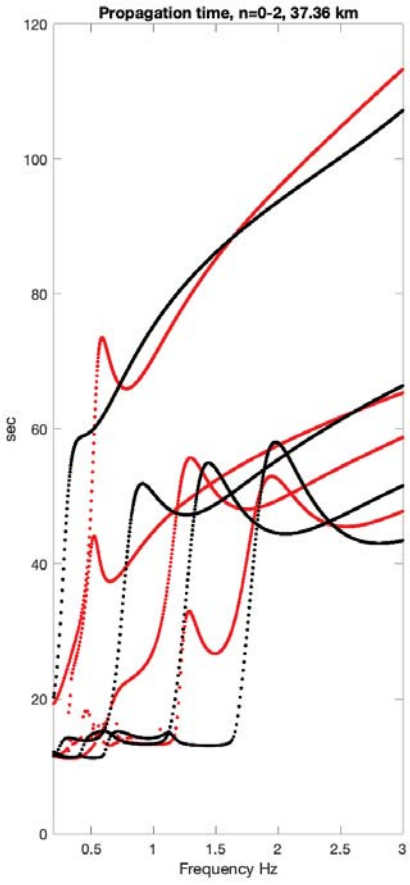
Propagation time, n=0-2, 37.36 km
sec
120
100
80
60
40
20
0
0.5
1
1.5
2
2.5
3
Frequency Hz

Figure 4.

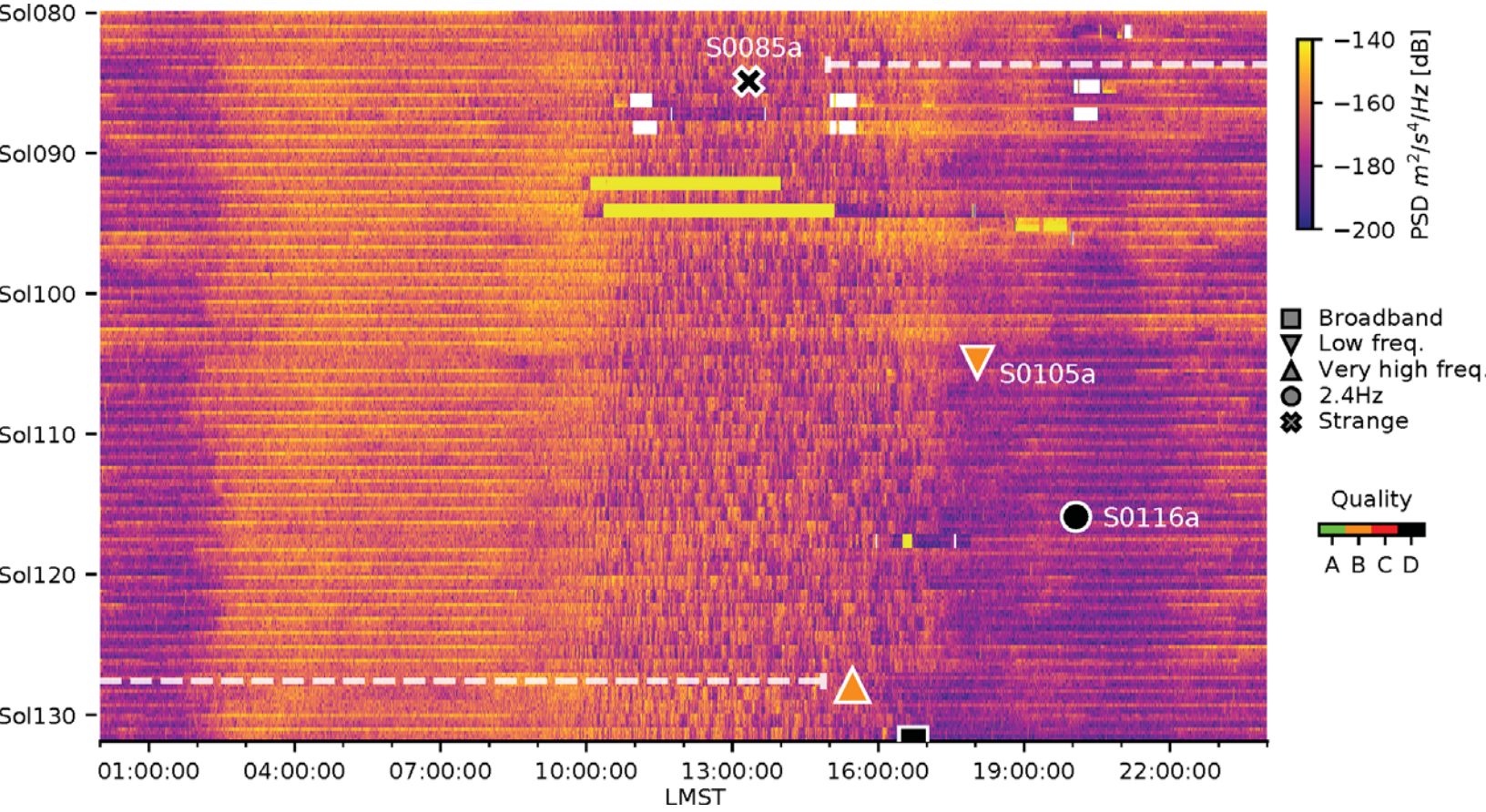
Sol080
Sol090
Sol100
Sol110
Sol120
Sol130
S0085a
S0105a
S0116a
01:00:00
04:00:00
07:00:00
10:00:00
13:00:00
16:00:00
19:00:00
22:00:00
LMST
−140
−160
−180
−200
PSD $m^2/s^4/Hz$ [dB]
Broadband
Low freq.
Very high freq.
2.4Hz
Strange
Quality
A B C D

Figure 5.

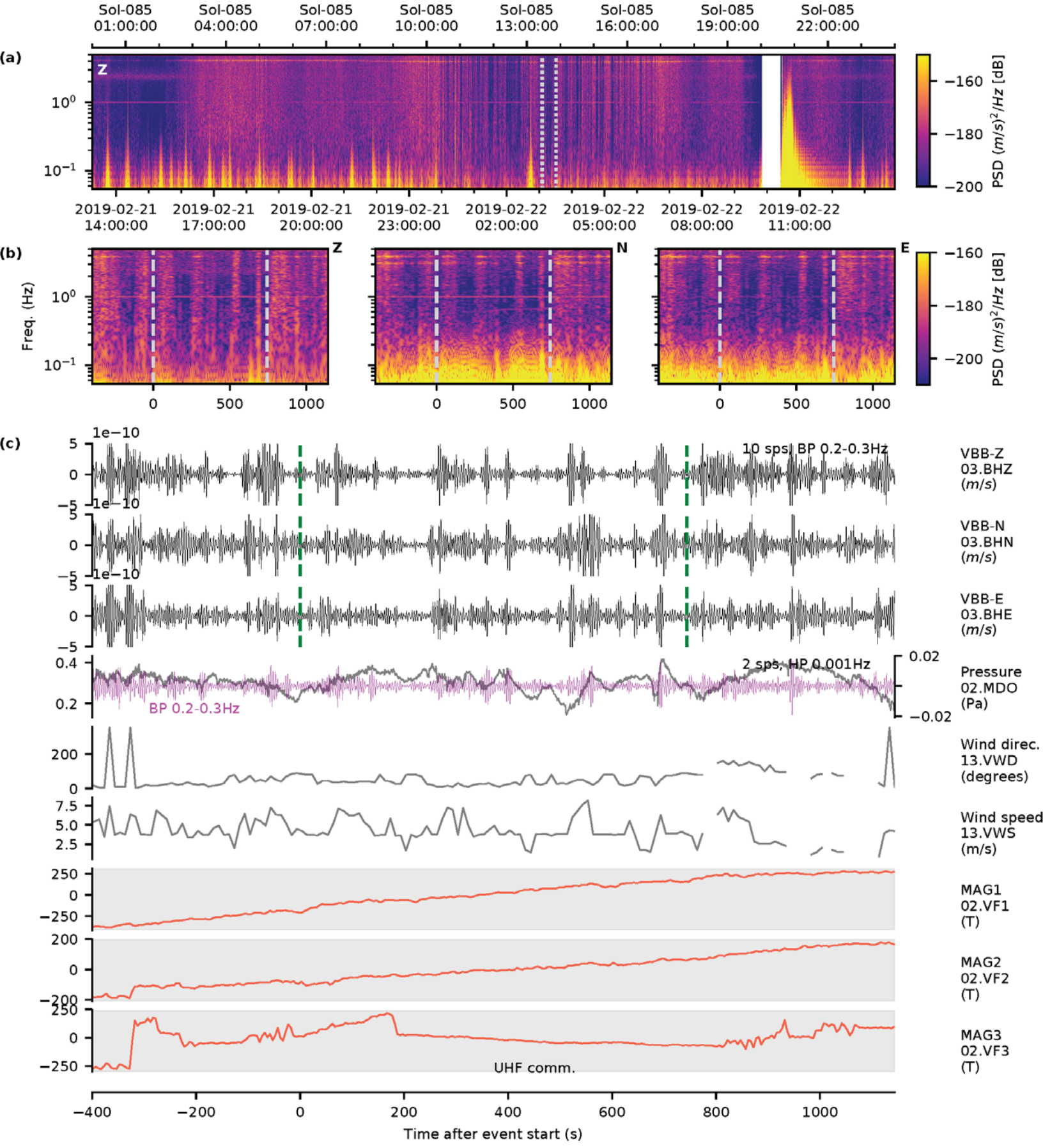
(a)
Sol-085 01:00:00
Sol-085 04:00:00
Sol-085 07:00:00
Sol-085 10:00:00
Sol-085 13:00:00
Sol-085 16:00:00
Sol-085 19:00:00
Sol-085 22:00:00
Z
10^0
10^{-1}
2019-02-21 14:00:00
2019-02-21 17:00:00
2019-02-21 20:00:00
2019-02-21 23:00:00
2019-02-22 02:00:00
2019-02-22 05:00:00
2019-02-22 08:00:00
2019-02-22 11:00:00
−160
−180
−200
PSD $(m/s)^2/Hz$ [dB]
(b)
Freq. (Hz)
Z
N
E
0
500
1000
(c)
1e−10
10 sps, BP 0.2-0.3Hz
VBB-Z
03.BHZ
(m/s)
VBB-N
03.BHN
(m/s)
VBB-E
03.BHE
(m/s)
2 sps, HP 0.001Hz
BP 0.2-0.3Hz
0.02
−0.02
Pressure
02.MDO
(Pa)
Wind direc.
13.VWD
(degrees)
Wind speed
13.VWS
(m/s)
MAG1
02.VF1
(T)
MAG2
02.VF2
(T)
MAG3
02.VF3
(T)
UHF comm.
−400
−200
0
200
400
600
800
1000
Time after event start (s)

Figure 6.

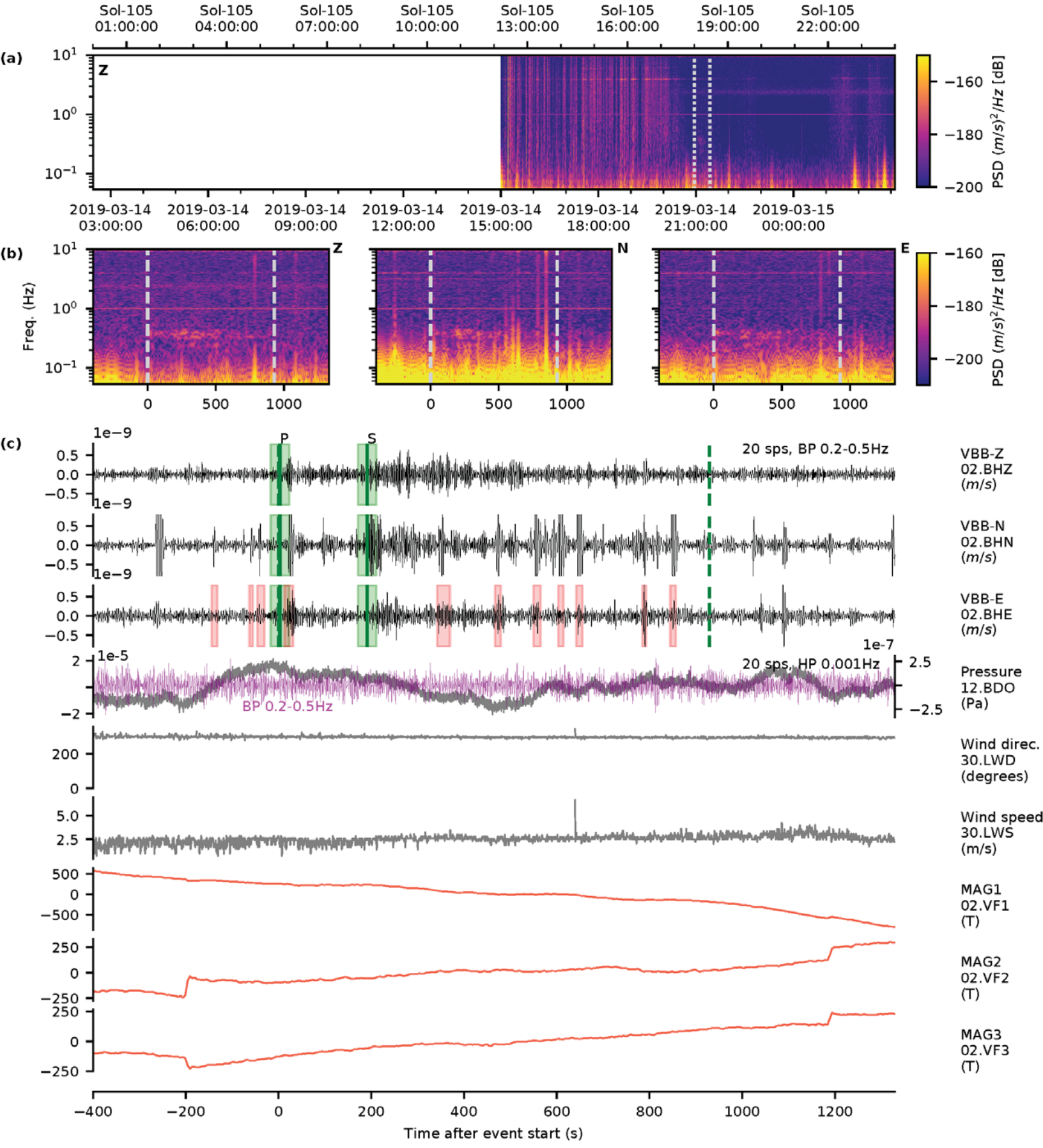
(a)
Sol-105 01:00:00
Sol-105 04:00:00
Sol-105 07:00:00
Sol-105 10:00:00
Sol-105 13:00:00
Sol-105 16:00:00
Sol-105 19:00:00
Sol-105 22:00:00
Z
2019-03-14 03:00:00
2019-03-14 06:00:00
2019-03-14 09:00:00
2019-03-14 12:00:00
2019-03-14 15:00:00
2019-03-14 18:00:00
2019-03-14 21:00:00
2019-03-15 00:00:00
PSD (m/s)²/Hz [dB]
(b)
Freq. (Hz)
Z
N
E
(c)
P
S
20 sps, BP 0.2-0.5Hz
VBB-Z 02.BHZ (m/s)
VBB-N 02.BHN (m/s)
VBB-E 02.BHE (m/s)
20 sps, HP 0.001Hz
BP 0.2-0.5Hz
Pressure 12.BDO (Pa)
Wind direc. 30.LWD (degrees)
Wind speed 30.LWS (m/s)
MAG1 02.VF1 (T)
MAG2 02.VF2 (T)
MAG3 02.VF3 (T)
Time after event start (s)

Figure 7.

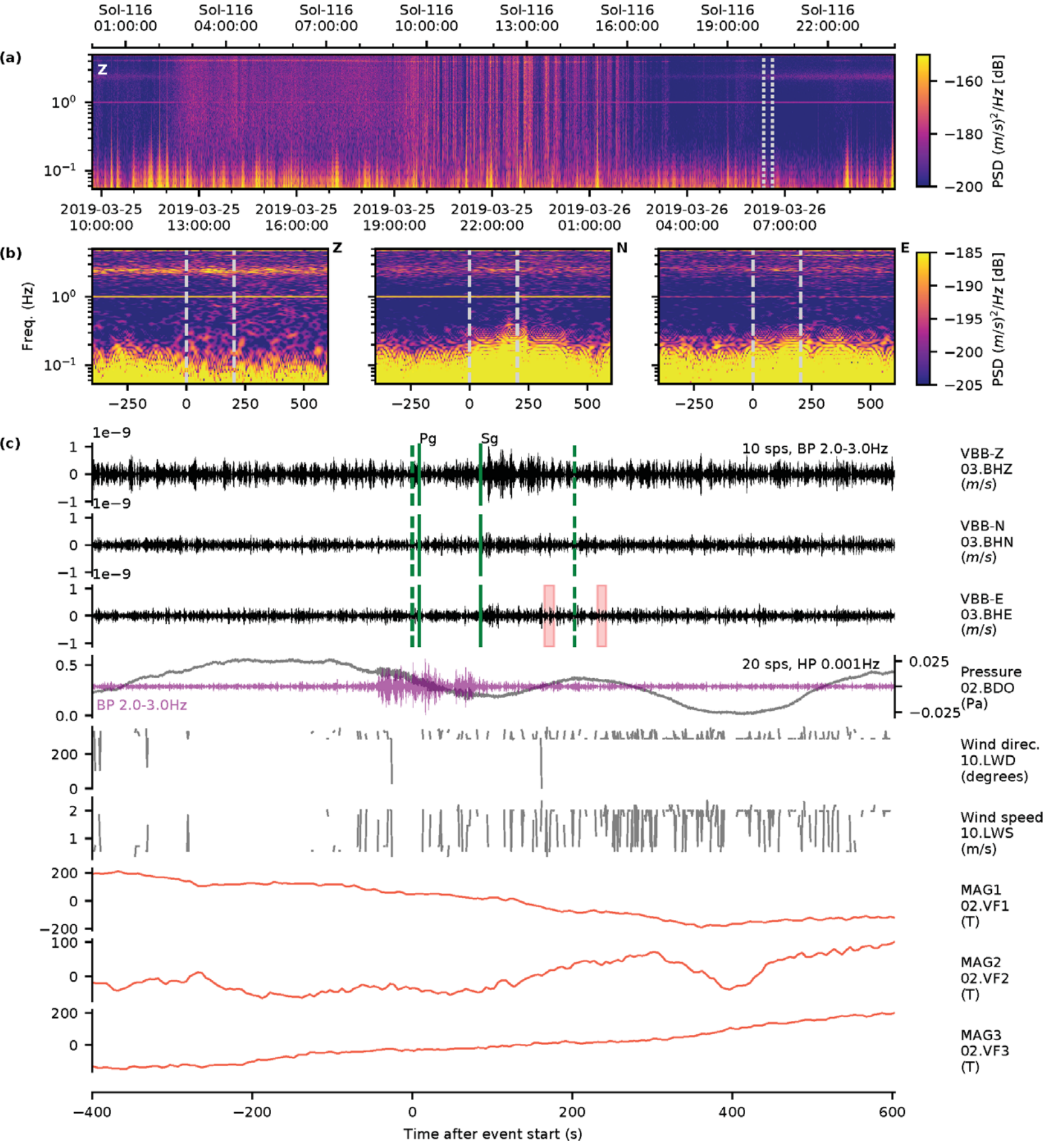
(a)
Sol-116 01:00:00
Sol-116 04:00:00
Sol-116 07:00:00
Sol-116 10:00:00
Sol-116 13:00:00
Sol-116 16:00:00
Sol-116 19:00:00
Sol-116 22:00:00
Z
10^0
10^{-1}
2019-03-25 10:00:00
2019-03-25 13:00:00
2019-03-25 16:00:00
2019-03-25 19:00:00
2019-03-25 22:00:00
2019-03-26 01:00:00
2019-03-26 04:00:00
2019-03-26 07:00:00
−160
−180
−200
PSD $(m/s)^2/Hz$ [dB]
(b)
Freq. (Hz)
Z
N
E
−250
0
250
500
−185
−190
−195
−200
−205
PSD $(m/s)^2/Hz$ [dB]
(c)
1e−9
Pg
Sg
10 sps, BP 2.0-3.0Hz
VBB-Z
03.BHZ
(m/s)
VBB-N
03.BHN
(m/s)
VBB-E
03.BHE
(m/s)
20 sps, HP 0.001Hz
BP 2.0-3.0Hz
0.025
−0.025
Pressure
02.BDO
(Pa)
Wind direc.
10.LWD
(degrees)
Wind speed
10.LWS
(m/s)
MAG1
02.VF1
(T)
MAG2
02.VF2
(T)
MAG3
02.VF3
(T)
−400
−200
0
200
400
600
Time after event start (s)

Figure 8.

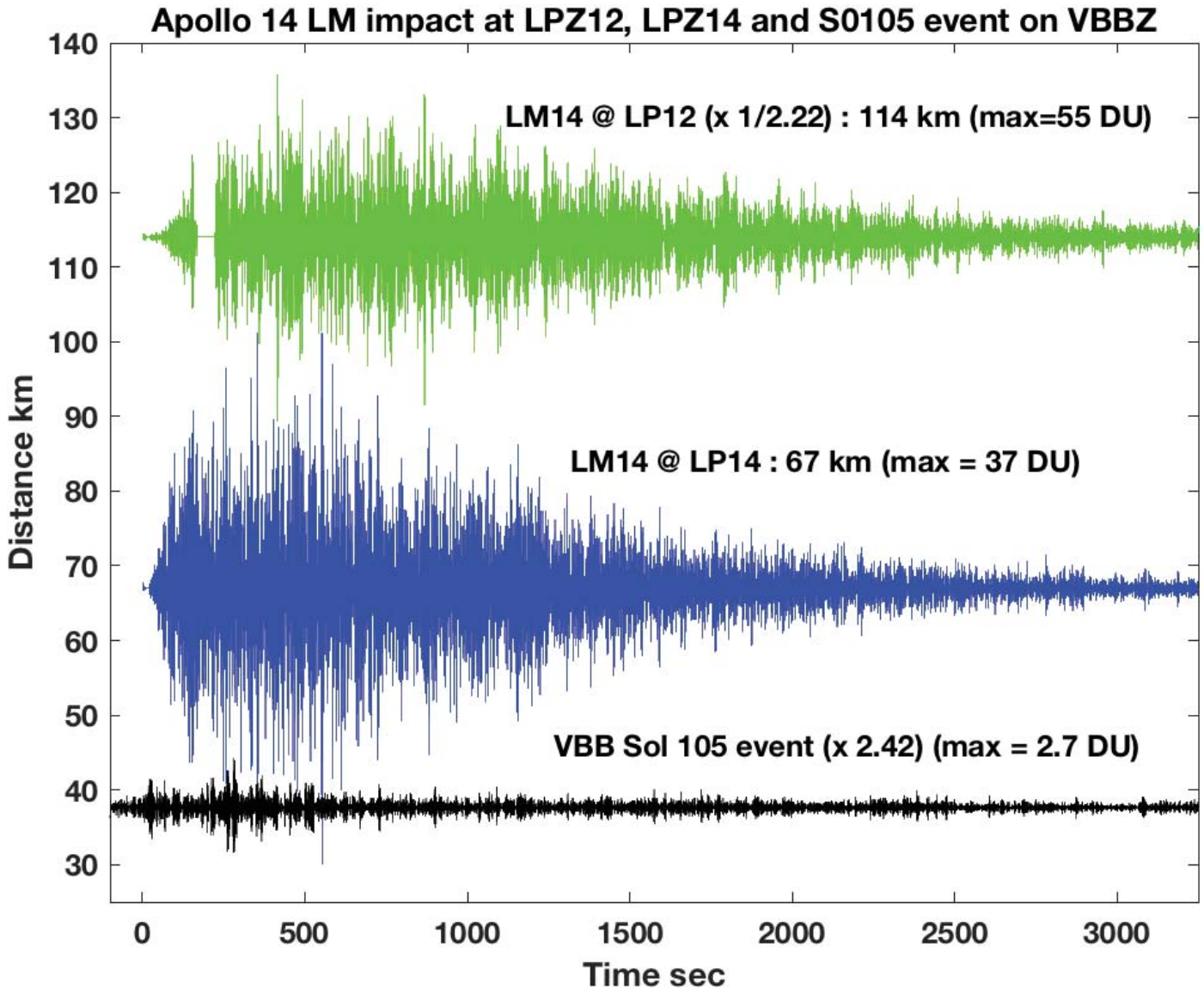
Apollo 14 LM impact at LPZ12, LPZ14 and S0105 event on VBBZ
LM14 @ LP12 (x 1/2.22) : 114 km (max=55 DU)
LM14 @ LP14 : 67 km (max = 37 DU)
VBB Sol 105 event (x 2.42) (max = 2.7 DU)
Distance km
Time sec
140
130
120
110
100
90
80
70
60
50
40
30
0
500
1000
1500
2000
2500
3000